

San Jose State University

From the Selected Works of Aaron J. Romanowsky

May, 2016

The SLUGGS survey*: exploring the globular cluster systems of the Leo II group and their global relationships

Sreeja S. Kartha, *Swinburne University of Technology*
Duncan A. Forbes, *Swinburne University of Technology*
Adebusola B. Alabi, *Swinburne University of Technology*
Jean P. Brodie, *University of California Observatories*
Aaron J. Romanowsky, *San Jose State University*, et al.



Available at: https://works.bepress.com/aaron_romanowsky/93/

The SLUGGS survey*: exploring the globular cluster systems of the Leo II group and their global relationships

Sreeja S. Kartha,^{1★} Duncan A. Forbes,¹ Adebisola B. Alabi,¹ Jean P. Brodie,² Aaron J. Romanowsky,^{2,3} Jay Strader,⁴ Lee R. Spitler,^{5,6} Zachary G. Jennings² and Joel C. Roediger⁷

¹Centre for Astrophysics & Supercomputing, Swinburne University, Hawthorn VIC 3122, Australia

²University of California Observatories, 1156 High St., Santa Cruz, CA 95064, USA

³Department of Physics and Astronomy, San José State University, One Washington Square, San Jose, CA 95192, USA

⁴Department of Physics and Astronomy, Michigan State University, East Lansing, MI 48824, USA

⁵Macquarie University, Macquarie Park, Sydney, NSW 2113, Australia

⁶Australian Astronomical Observatory, PO Box 915, North Ryde, NSW 1670, Australia

⁷NRC Herzberg Astronomy & Astrophysics, Victoria, BC V9E 2E7, Canada

Accepted 2016 January 20. Received 2016 January 20; in original form 2015 July 23

ABSTRACT

We present an investigation of the globular cluster (GC) systems of NGC 3607 and NGC 3608 as part of the ongoing SLUGGS (SAGES Legacy Unifying Globulars and GalaxieS) survey. We use wide-field imaging data from the Subaru telescope in the g , r and i filters to analyse the radial density, colour and azimuthal distributions of both GC systems. With the complementary kinematic data obtained from the Keck II telescope, we measure the radial velocities of a total of 81 GCs. Our results show that the GC systems of NGC 3607 and NGC 3608 have a detectable spatial extent of ~ 15 and 13 galaxy effective radii, respectively. Both GC systems show a clear bimodal colour distribution. We detect a significant radial colour gradient for the GC subpopulations in both galaxies. NGC 3607 exhibits an overabundance of red GCs on the galaxy minor axis and NGC 3608 shows a misalignment in the GC subpopulation position angles with respect to the galaxy stellar component. With the aid of literature data, we discuss several relationships between the properties of GC systems and their host galaxies. A one-to-one relation between the ellipticities of red GCs and the galaxy stellar light emphasizes the evolutionary similarities between them. In our sample of four slowly rotating galaxies with kinematically decoupled cores, we observe a higher ellipticity for the blue GC subpopulation than their red counterparts. Also, we notice the flattening of negative colour gradients for the blue GC subpopulations with increasing galaxy stellar mass. Finally, we discuss the formation scenarios associated with the blue GC subpopulation.

Key words: galaxies: elliptical and lenticular, cD – galaxies: individual: NGC 3605 – galaxies: individual: NGC 3607 – galaxies: individual: NGC 3608 – galaxies: star clusters: individual.

1 INTRODUCTION

To better understand the formation of early-type galaxies (ETGs), it is useful to study their oldest stellar components, such as globular clusters (GCs). GCs are mostly old (~ 10 Gyr; Strader et al. 2005), luminous ($\geq 10^5 L_{\odot}$; Brodie et al. 2011) and compact ($R_e \sim 3$ pc) star clusters. Establishing connections between the properties of GC systems and their host galaxies can help in understanding the formation of GC systems and hence their parent galaxies.

In almost all massive galaxies, GC systems are found to be bimodal in colour (Larsen et al. 2001; Peng et al. 2006; Kim et al. 2013; Hargis & Rhode 2014). Transforming colours to metallicity connects this bimodality with two stages of GC formation. The colour/metallicity distribution peaks are represented by blue/metal-poor and red/metal-rich GC subpopulations (Brodie et al. 2012). In a recent work, Forbes et al. (2015) determined the mean ages of blue and red GC subpopulations as 12.2–12.8 and 11.5 Gyr, respectively, suggesting that both subpopulations are very old. However, the two peaks differ in colour (e.g. 0.8 and 1.1 in $(g - i)$) and metallicity (i.e. $[Z/H]$ peaks at -1.5 and -0.4 dex) values. Other properties of the two subpopulations differ such as azimuthal distribution, spatial distribution, radial colour distribution (Strader et al. 2011; Park & Lee

* <http://sluggs.swin.edu.au/>

★ E-mail: skartha@astro.swin.edu.au

Table 1. Basic data for the target galaxies: NGC 3605, NGC 3607 and NGC 3608. Right ascension and declination (J2000) are taken from NASA/IPAC Extragalactic Database (NED). The galaxy distance, effective radius, heliocentric velocity, position angle and ellipticity, for NGC 3607 and NGC 3608, are from Brodie et al. (2014). For NGC 3605, the galaxy distance, effective radius and heliocentric velocity are taken from Cappellari et al. (2011), whereas the position angle and ellipticity are obtained from HyperLeda (Paturel et al. 2003). Total V -band magnitudes are obtained from de Vaucouleurs et al. (1991). The extinction correction for the V band is calculated from Schlegel, Finkbeiner & Davis (1998). The absolute magnitude is derived from the V -band magnitude, distance and the extinction correction.

Name	RA (h:m:s)	Dec. (°:′:″)	Type	D (Mpc)	V_T (mag)	A_v (mag)	M_V^T (mag)	R_e (arcsec)	PA (°)	ϵ	Vel (km s ⁻¹)
NGC 3605	11:16:46.6	+18:01:02	E4–5	20.1	12.15	0.07	−19.36	17	19	0.40	661
NGC 3607	11:16:54.6	+18:03:06	S0	22.2	9.89	0.07	−21.86	39	125	0.13	942
NGC 3608	11:16:58.9	+18:08:55	E1–2	22.3	10.76	0.07	−20.98	30	82	0.20	1226

2013) and also kinematics (Pota et al. 2013). Three scenarios have been suggested to explain the formation of these two distinct GC subpopulations: major merger (Ashman & Zepf 1992), multi-phase collapse (Forbes et al. 1997) and accretion (Côté, Marzke & West 1998; Côté et al. 2000). See Brodie & Strader (2006) and Harris (2010) for reviews. Many cosmological simulations of hierarchical galaxy formation have been used to investigate the characteristics of GC systems (physical, dynamical, chemical, etc.) in ETGs (Beasley et al. 2002; Bekki et al. 2005, 2008; Griffen et al. 2010; Muratov & Gnedin 2010; Katz & Ricotti 2013; Tonini 2013; Gnedin, Ostriker & Tremaine 2014; Trenti, Padoan & Jimenez 2015).

In order to associate the formation of different GC subpopulations with galaxy formation events, we explore the radial and azimuthal distributions of both subpopulations and compare with galaxy stellar light. Generally, the radial distribution of blue GCs is found to be more extended than that of both the red GC subpopulation and the galaxy stellar light. The red GC subpopulation is similar in radial distribution to the galaxy light (Bassino, Richtler & Dirsch 2006a; Strader et al. 2011), whereas the profiles of the blue GC subpopulation show similarities with the X-ray surface brightness profiles (Forbes, Ponman & O’Sullivan 2012). The radially extended blue GC subpopulation residing in galaxy haloes suggests that they are very old stellar components formed early in an *in situ* dissipative collapse galaxy formation scenario, or accreted later, into the galaxy outskirts, in galaxy build-up by minor merger formation scenario. The similarity of red GCs with the galaxy stellar light supports coeval formation, but their origin (from the enriched gas of a parent galaxy or from accreted gas) is not clear.

Park & Lee (2013) studied the azimuthal distribution of GC systems in 23 ETGs using the data from the Advanced Camera for Surveys (ACS) mounted on the *Hubble Space Telescope* (*HST*). They found that the ellipticities of the red GC subpopulation match the galaxy stellar light ellipticities with a one-to-one correspondence. They also found that blue GC subpopulations show a similar but less tight relation. Wang et al. (2013) using the ETGs, from the ACS Virgo Cluster Survey (VCS), concluded that both red and blue GC subpopulations align in position angle with the galaxy stellar light, although in a weaker way for blue GC subpopulations. Several single galaxy studies concluded that the galaxy stellar light is mimicked by red GC subpopulation in position angle and ellipticity, but the blue GC subpopulation is differently distributed (e.g. NGC 4365: Blom, Spitler & Forbes 2012; NGC 5813: Hargis & Rhode 2014; NGC 720, NGC 1023: Kartha et al. 2014).

The decreasing mean colour of GC subpopulations with increasing galactocentric radius is a key diagnostic observation (Bassino et al. 2006b; Harris 2009; Arnold et al. 2011; Faifer et al. 2011; Forbes et al. 2011; Blom et al. 2012; Usher et al. 2013; Hargis & Rhode 2014). More specifically, the degree of steepness allows us to distinguish between two different formation processes, dissipation

and accretion/merger (Tortora et al. 2010). Recently, Forbes et al. (2011) studied the colour gradient for NGC 1407 GC subpopulations and found that both GC subpopulations have a steep negative gradient within ~ 8.5 effective radii (R_e) and a constant colour to larger radii. They explained this colour trend as being compatible with two-phase galaxy formation (Oser et al. 2010). This implies that the inner GCs are formed during a dissipative collapse phase, whereas the outer GCs are acquired during late accretion/mergers. Thus, exploring the radial colour distribution can reveal clues about formation events that happened in the host galaxy’s history.

The layout of this paper is as follows. A brief literature review of the target galaxies is presented in Section 1.1. Section 2 describes the observations, data reduction techniques and initial analysis of imaging and spectroscopic data. Sections 3 and 4 present the GC selection techniques and methods used to select the GC systems of individual galaxies. A detailed analysis of various GC system distributions (radial density, colour and azimuthal) for the selected GC systems is presented in Section 5. In Section 6, we discuss connections between the characteristics of galaxy stellar light and GC systems followed, in Section 7, by the conclusion.

1.1 NGC 3607 and NGC 3608 in the Leo II group

Here, we focus on the GC systems of the Leo II group. NGC 3607 and NGC 3608 are the brightest ETGs in the Leo II group. NGC 3607 is a near face-on lenticular galaxy, while NGC 3608 is an E1–2 elliptical galaxy. In the same system, there is a third galaxy, NGC 3605, which is a low-mass galaxy of E4–5 morphology. Table 1 presents the main characteristics of the three galaxies with NGC 3607 as the central galaxy in the group. NGC 3608 and NGC 3605 are situated at a distance of 6 arcmin north-east and 2 arcmin south-west from NGC 3607. Kundu & Whitmore (2001a,b) investigated the GC systems of 57 ETGs including NGC 3607 and NGC 3608 using *HST*/Wide-Field Planetary Camera 2 (WFPC2) data in V and I filters. For these galaxies, they detected 130 and 370 GCs, respectively, from single pointing imaging. They did not find a sign of a bimodal colour distribution in either galaxy.

With the same *HST*/WFPC2 data, Lauer et al. (2005) investigated the surface brightness profiles of NGC 3607 and NGC 3608. They mentioned that NGC 3607 contains a symmetric, old and tightly wrapped outer dusty disc to which a second disc is settling in a perpendicular direction. They explained this observation as an infall of gas directly to the centre of galaxy with no interaction with the outer disc. They also detected the remnants of a pre-existing dusty disc in NGC 3608. Terlevich & Forbes (2002) derived the ages of 150 galaxies using the spectral line indices and found 5.8, 3.6 and 10 Gyr ages for NGC 3605, NGC 3607 and NGC 3608, respectively. Later, Ricketts, Pastoriza & Bonatto (2009) investigated the

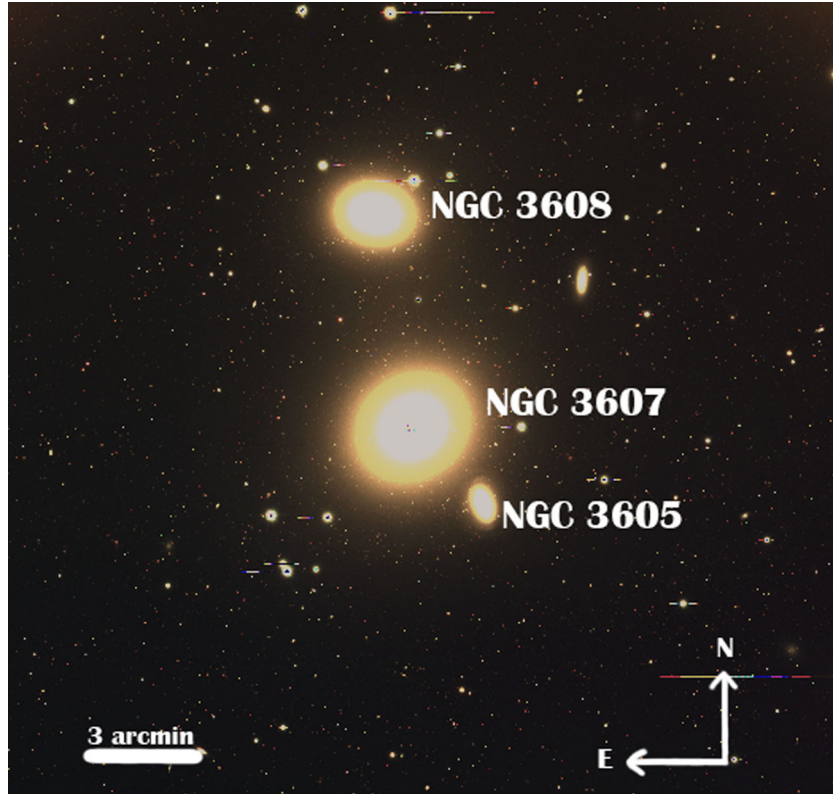


Figure 1. A mosaic image showing the central 28×23 arcmin² area of the Leo II galaxy group. This Subaru/Suprime-Cam image is a combination of g , r and i filters. The target galaxies are labelled. The central galaxy, NGC 3607, is at a distance of 22.2 Mpc implying $1 \text{ arcsec} = 0.107 \text{ kpc}$.

metallicity distribution, stellar population and ionized gas in NGC 3607 using long-slit spectroscopy. They found stellar components ranging in age from 1 to 13 Gyr between the centre and a 30 arcsec radius of the galaxy’s centre. As part of the ATLAS^{3D} survey, McDermid et al. (2015) determined the mass-weighted ages for NGC 3605, NGC 3607 and NGC 3608 as 8.1 ± 0.8 , 13.5 ± 0.7 and 13.0 ± 0.7 Gyr, respectively. Also, from the ATLAS^{3D} survey Duc et al. (2015) studied these galaxies using the deep multi-band images from the Canada–France–Hawaii Telescope. They mentioned that NGC 3607 and NGC 3608 are interacting galaxies with the presence of weak dust lanes and ripples.

Based on the *ROSAT* data, two peaks were detected in diffuse hot X-rays on NGC 3607 and NGC 3608 (Mulchaey et al. 2003). They proposed that the two galaxies are undergoing a merger. Later, Forbes et al. (2006a) detected an extended diffuse X-ray emission around the Leo II group.

The GC systems of the ETGs at the centre of the Leo II group have not yet been studied using wide-field imaging data. As part of the SLUGGS (SAGES Legacy Unifying Globulars and GalaxieS) survey (Brodie et al. 2014), we obtained wide-field data in three optical filters covering the central region of the Leo II group using the Suprime-Cam instrument on the Subaru telescope. With the aid of the imaging and spectroscopic data, we aim to understand the properties of the GC systems associated with each galaxy.

2 DATA

2.1 Observations and reduction techniques

Photometric data for the Leo II group were obtained using the Subaru Prime Focus Camera (Suprime-Cam; Miyazaki et al. 2002)

mounted on the 8 m Subaru telescope. The Suprime-Cam imager consists of 10 CCDs with individual sizes of 2048×4096 pixels and a pixel scale of 0.202 arcsec, covering a maximum sky area of 34×27 arcmin². Wide-field images were obtained during 2011 January 3 and 4. The sky conditions were good with an average seeing of ~ 0.81 , 0.80 and 0.80 for the g , r , i filters, respectively. Multiple exposures in a dithered pattern were taken to fill the gaps between individual CCDs. In g , r and i filters, the total exposure times were 3743, 1560 and 1200 s, respectively.

The individual exposures were reduced and combined using the Suprime-Cam Deep Field Reduction package 2 (SDFRED2; Ouchi et al. 2004) for each of the three filters. The pre-processing of images included flat-fielding, distortion corrections and atmospheric dispersion corrections. The pipeline also features custom-made modifications to improve the sky subtraction and alignment between multiple exposures. We employed SExtractor (Bertin & Arnouts 1996)¹ and MONTAGE² for the alignment process. All point sources 3σ above the background level are identified on each CCD image using SExtractor. The positions of these point sources are matched with a reference catalogue (here we use the Sloan Digital Sky Survey, SDSS) to create an astrometric solution. The astrometric solution is used by the MONTAGE program to align and combine the individual images, generating mosaic images in the three filters. A combination of g , r and i filter mosaic images is shown in Fig. 1.

We also obtained a single pointing covering the central region of NGC 3607 from the Hubble Legacy Archive. This was taken in the *F814W* (I) filter using the ACS instrument. The Wide-Field Channel

¹ <http://www.astromatic.net/software/>

² <http://montage.ipac.caltech.edu/index.html>

on the ACS consists of two 2048×4096 CCDs with a 0.049 arcsec pixel scale, and 3.37×3.37 arcmin² field of view. A custom-made pipeline (for detailed explanation, see Spitler et al. 2006) is employed to reduce the ACS data. The pipeline provides source positions and half-light radii for all the detected sources, which are utilized for a preliminary selection of GCs in the Subaru/Suprime-Cam imaging (see Section 3).

Complementary spectroscopic data were obtained using the DEep Imaging Multi-Object Spectrograph (DEIMOS; Faber et al. 2003) on the Keck II telescope. The field of NGC 3607 was targeted on five nights during 2013 January 10–12 and 2014 January 26 and 27 as part of the SLUGGS survey. We used five slit masks for good azimuthal coverage and the seeing per night was $0.87 \leq \text{FWHM} \leq 1.15$ arcsec with a total exposure time of ~ 10 h. DEIMOS was used with 1200 l/mm grating centred on 7800 \AA , with slit widths of 1 arcsec. In this way, we have a wavelength coverage from 6500 to 8700 \AA and spectral resolution of $\sim 1.5 \text{ \AA}$. We reduced the raw spectra using the IDL SPEC2D reduction pipeline together with dome flats and arc lamp spectra. The pipeline produces sky-subtracted GC spectra that cover the CaT absorption lines in the near-infrared ($8498, 8542, 8662 \text{ \AA}$) and H α line at 6563 \AA (where possible).

We obtain the radial velocities from our science spectra using the FXCOR task in IRAF by measuring the Doppler shift of the CaT lines, cross-correlating each Fourier transformed science spectrum with the Fourier transformed spectra of 13 Galactic template stars. In practice, we require that the strongest CaT lines ($8542, 8662 \text{ \AA}$) be present and where possible the H α line as well. Where the lines are not properly defined, but the velocity is consistent with either galaxy, the GC is classified as marginal. Objects with velocities less than 350 km s^{-1} are classified as Galactic stars and those with velocities greater than 1800 km s^{-1} as background galaxies. Our final catalogue has 75 GCs and 7 ambiguous objects (see Table A1 in Appendix A). Here, ‘ambiguous’ denotes that either the velocity or position has a mismatch with the target galaxies, but it has confirmed characteristics of a GC.

2.2 Photometry

Before carrying out any photometric analysis, the galaxy light was subtracted in each of the three mosaic images. The two large galaxies are individually modelled using IRAF task ELLIPSE with the centre of the galaxy, the major axis position angle (PA) and the ellipticity (ϵ) as free fitting parameters. During the fitting process, the bright stars were masked before modelling the galaxy light. The best-fitting galaxy model produces radial profiles of surface brightness, position angle and ellipticity measurements for both the galaxies. We made use of galaxy light subtracted images to improve the source detection in the central regions of target galaxies.

We utilized SExtractor for source identification and photometry. We instructed SExtractor to identify a probable source only if it has a minimum of 5 adjacent pixels with a flux higher than 3σ above the local background. SExtractor estimates the total instrumental magnitudes for the detected sources using Kron radii (Kron 1980) in the automatic aperture magnitude mode. It provides an output list of point sources with position and magnitude. As standard stars were not observed for zero-point calibration, we exploited the bright stars ($i < 22$) present in the galaxy field. A match between these bright stars and the SDSS catalogue (Data Release 7 version) was used for the flux calibration in all three mosaic images. Photometric zero-point magnitudes in three filters are derived from the best-fitting linear relationship between the instrumental magnitudes of bright stars and calibrated magnitudes from the SDSS catalogue.

Estimated zero-points in the g, r, i bands are $28.68 \pm 0.08, 28.92 \pm 0.12, 28.78 \pm 0.15$ mag, respectively. All magnitudes have had the zero-point correction applied. The galaxy photometry is corrected for Galactic extinction using the dust extinction maps from Schlegel et al. (1998). Hereafter, all the magnitudes and colours cited are extinction corrected.

3 GC SELECTION

The large galaxies, NGC 3607 and NGC 3608, are at an assumed distance of 22.2 ± 0.1 Mpc (Brodie et al. 2014) and NGC 3605 taken to be 20.1 Mpc (Cappellari et al. 2011). For GC identification, a match of object positions between the three bands is carried out at first, in order to eliminate the false detections. Afterwards a separation between extended objects (galaxies) and point source objects (both GCs and stars) is incorporated. This separation is based on the surplus light detected beyond the extraction aperture. Objects showing large difference between the extraction aperture and an outer aperture are considered as extended sources and are removed (see Kartha et al. 2014 for details).

We employ a colour–colour selection as the next step to identify the GC candidates. To aid this selection, we used the position and half-light radius of the sources from the HST/ACS data. An upper limit of ~ 9 pc at the distance of NGC 3607, for GC candidature, is applied, and the selected objects are visually verified. A positional match between the Subaru objects and the GCs selected on the HST/ACS image is carried out, and then the half-light radius is attached to the Subaru list for the common objects. Hence, we create a list of probable GCs with their positions, three magnitudes from the Subaru/Suprime-Cam data, and half-light radii from the HST/ACS data. From earlier studies, e.g. fig. 6 in Blom et al. (2012) and fig. 3 in Pota et al. (2013), it is evident that the GCs populate a particular region in the colour–colour diagram. With the above list, we identify the locus of GCs in $(r-i)$ versus $(g-i)$ colour space, implementing similar procedures as explained in Spitler et al. (2008) and Blom et al. (2012). The GC candidates, along with neighbouring objects showing a 2σ deviation from the selected region, are chosen as final GC candidates. The selected GCs range over $0.6 < (g-i) < 1.4$, which corresponds to a metallicity range of $-1.94 < [Z/H] < 0.86$ using the empirical relation given in Usher et al. (2012). The upper and lower cut-offs in i -band magnitude are 20.4 and 24.4 mag, respectively. At the distance of NGC 3607, objects brighter than 20.4 mag include ultra-compact dwarfs (UCDs; Brodie et al. 2011), while the lower limit is 1 mag fainter than the turnover magnitude for the GC system. This final list of GC candidates includes ~ 1000 objects from NGC 3605, NGC 3607 and NGC 3608.

4 DEFINING THE GC SYSTEMS OF EACH GALAXY

We derive the stellar mass of NGC 3605 as $\log(M_*) = 10.76 M_\odot$ from the galaxy V -band magnitude (see Table 1) and the mass-to-light (M/L) ratio from Zepf & Ashman (1993). The extent of the GC system of NGC 3605 is calculated from the stellar mass in the empirical relation between GC system extent and the galaxy stellar mass (equation 7 in Kartha et al. 2014). A GC system extent of ~ 40 arcsec is derived from the calculation, and we assume a maximum of 1 arcmin extent for NGC 3605. We detect 10 objects in the 1 arcmin region around NGC 3605 and eliminate them from the following calculations. The surface density distribution of GCs around NGC 3605 has been investigated, and we find a constant GC

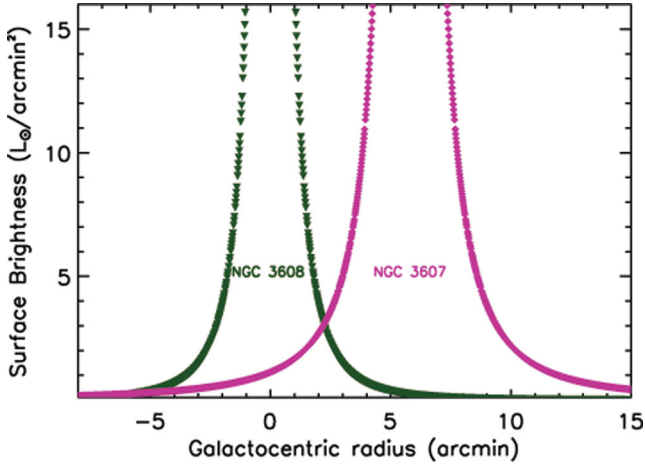


Figure 2. Surface brightness profiles for individual galaxies. The *i*-band profiles have been extracted using IRAF ELLIPSE task and extrapolated towards larger radii from the centres of NGC 3607 and NGC 3608. The negative to positive radius represents the declination axis centred on NGC 3608.

density, implying no contamination from NGC 3605 to the NGC 3607 or NGC 3608 GC systems.

The remaining GC candidates are a combination of objects from NGC 3607 and NGC 3608. In order to classify their individual GC systems, we invoke two methods, based on surface brightness and position angle of the host galaxies.

4.1 Surface brightness method

The galaxy light for both galaxies is modelled and extracted using the IRAF task ELLIPSE. The individual surface brightness profiles are fitted with Sérsic profiles (Graham & Driver 2005). We extrapolate these profiles to larger galactocentric radius (~ 15 arcmin) and use these extrapolated profiles to represent the stellar light profiles of individual galaxies to large radius. Fig. 2 shows the surface brightness profiles of NGC 3607 and NGC 3608. Based on the position of each GC, its membership probability is computed from the ratio of surface brightness of NGC 3607 to NGC 3608. Hereafter we refer to this as the surface brightness (SB) method. GCs with a probability greater than 55 per cent are counted as members of NGC 3607, while less than 50 per cent are classified as members of NGC 3608. The $6 R_e$ ellipses overlap around 55 per cent SB probability (see Fig. 3). We classify the GCs with probability between 55 and 50 per cent as ambiguous objects.

4.2 Major axis method

We employed a second method called the major axis (hereafter MA) method, to separate the GC systems of the two galaxies. In this method, we divided the GCs along the photometric major axis (125 and 82 deg for NGC 3607 and NGC 3608, respectively) and selected the hemisphere pointing away from the other galaxy. Thus, the selection of GCs for NGC 3607 includes GCs in the position angles 125 to 305 deg and for NGC 3608 GCs from 0 to 82 and 262 to 360 deg. This method excludes the region of maximum tidal interaction between the two galaxies. Coccato et al. (2009) adopted a similar method for disentangling the planetary nebulae (PNe) of NGC 3608. To eliminate the contaminants from NGC 3607, they excluded the PNe on the southern side of NGC 3608, which is equivalent to the MA method used here.

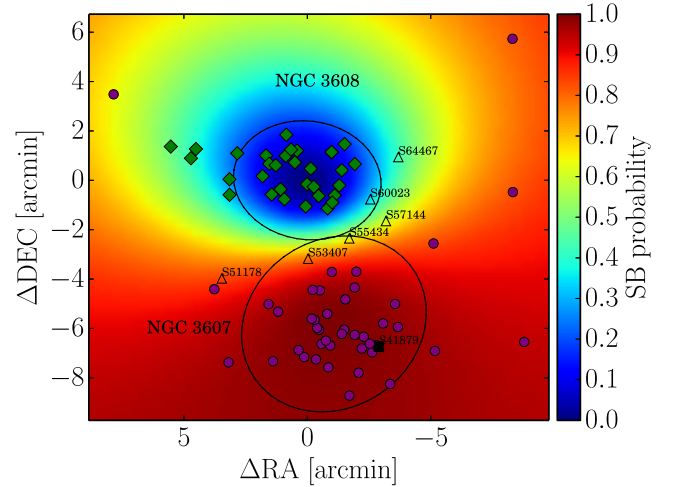


Figure 3. Spectroscopically confirmed GCs of NGC 3607 and NGC 3608. The galaxy centres for NGC 3608 and NGC 3607 are, respectively, at coordinates (0,0) and $(-1.1, -5.8)$. The magenta circles and green diamonds represent the GC members of NGC 3607 and NGC 3608, while open triangles and black square represent ambiguous GCs (with IDs denoted) and one extreme object (ID: S41879). The colour map in the background represents the membership probability from the surface brightness and the colour coding is shown to the right. The black ellipses represent six effective radii for the two galaxies with their respective ellipticity and position angle of the galaxy stellar light (refer to Table 1).

4.3 Analysis of kinematic data

We obtained the radial velocity measurements for 82 (confirmed plus marginal) GCs in the field of the Leo II group. The galaxy systemic velocities for NGC 3607 and NGC 3608 are 942 and 1226 km s^{-1} (Brodie et al. 2014), respectively. To assign the membership of GCs to individual galaxies, we performed a biweight estimator distribution (following Walker et al. 2006) based on the right ascension, declination and line-of-sight velocity of each GC. The GCs within 2σ (σ is the standard deviation calculated from the velocity distribution) from the central galaxy velocity are assigned membership to the corresponding galaxy, while keeping marginal members as velocities between 2σ and 3σ . Fig. 3 displays positions of spectroscopically confirmed GCs on an SB probability map. The background map shows the SB probability used in the separation of GCs (see Section 4.1). The positions of individual galaxy GCs (as determined using velocities) fall on the same region derived from the SB method, confirming the robustness of the SB probability method for classifying the GCs. The distribution gives 43 and 32 GCs, respectively, as NGC 3607 and NGC 3608 members.

In addition, we classified the seven ambiguous objects as six GCs and one extreme member. The extreme member S41879 has a velocity of $1822 \pm 22 \text{ km s}^{-1}$, but positionally it is projected near the centre of NGC 3607 (see Fig. 3) in the 2D map. Assuming that it lies at the distance of NGC 3607 ($D = 22.2$ Mpc), then it has $M_i = -9.97$ mag. From the line-of-sight velocity and $H_0 = 70 \text{ km s}^{-1} \text{ Mpc}^{-1}$, we calculate the distance as 26 Mpc and hence the magnitude $M_i = -10.31$ mag. This suggests that it is a possible UCD (see Brodie et al. 2011). To confirm this, we checked the *HST* image for an estimation of its size. Unfortunately, this object is placed in the central gap region of the *HST* pointing. We examined the Subaru image and found that the object is very

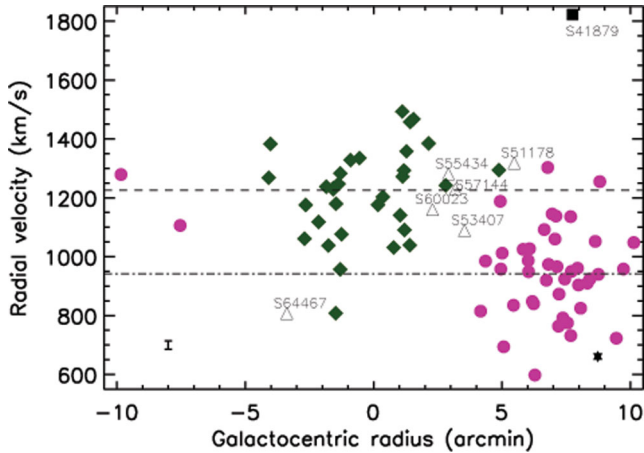


Figure 4. Velocity distribution of spectroscopically confirmed GCs as a function of radius with respect to NGC 3608. The NGC 3607 and NGC 3608 members are represented with magenta circles and green diamonds, while marginal GCs and one extreme object (ID: S41879) with open triangles and a filled square. The position of NGC 3605 is represented with a black star. The dot-dashed and the dashed horizontal lines represent the galaxy systemic velocities for NGC 3607 and NGC 3608, respectively. An average error of 14 km s^{-1} is shown at the lower left.

circular in shape. Another possibility is an intra-group GC, as it is blue ($g - i$) = 0.623, circular in shape and lies in the projected region between NGC 3607 and NGC 3605. With the above information, we suggest that this extreme object might be a background UCD or an intra-group GC. Eliminating this extreme object, we have 81 spectroscopically confirmed GCs for NGC 3607 and NGC 3608.

Fig. 4 shows the velocity distribution of GCs with galactocentric radius measured from the centre of NGC 3608. The six marginal GCs are labelled in Figs 3 and 4. Based on both these figures, we assign a membership for the marginal GCs. Note here that this manual membership assignment is unimportant for any broad conclusions of this study. S51178 is positionally close towards NGC 3607 with velocity $>1300 \text{ km s}^{-1}$. But according to the SB probability, this GC has >80 per cent probability to be associated with NGC 3607. Hence, considering these facts we assign it to NGC 3607 as GC44 (name given in Table A1). Based on the SB probability and velocity measurement, S53407 is assigned to NGC 3607 (GC45). The position of S64467 is close to NGC 3608 with 50 per cent probability, but having a velocity of 807 km s^{-1} supports a membership with NGC 3607 (GC46). S60023 has a 70 per cent probability with NGC 3608 and with a velocity of 1160 km s^{-1} . Hence, S60023 is a probable member of NGC 3608 (GC33). S55434 (GC34) and S57144 (GC35) are GCs with velocities 1281 and 1229 km s^{-1} , respectively. Both fall on the probability region of ~ 60 per cent for NGC 3607. However, a membership to NGC 3608 is allocated for these GCs based on the positional closeness and velocities. Hence, S60023, S55434, S57144 are NGC 3608 members and S51178, S64467, S53407 are NGC 3607 members. Finally, NGC 3608 and NGC 3607 have 35 and 46 spectroscopically confirmed GCs, respectively.

The mean velocities estimated from the GC systems of NGC 3607 and NGC 3608 are 963 and 1220 km s^{-1} , respectively, in good agreement with galaxy central velocities. Estimates of the GC system velocity dispersions for NGC 3607 and NGC 3608 are 167 and 147 km s^{-1} , respectively. Cappellari et al. (2013) found central velocity dispersions of 206.5 ± 10 and $169.0 \pm$

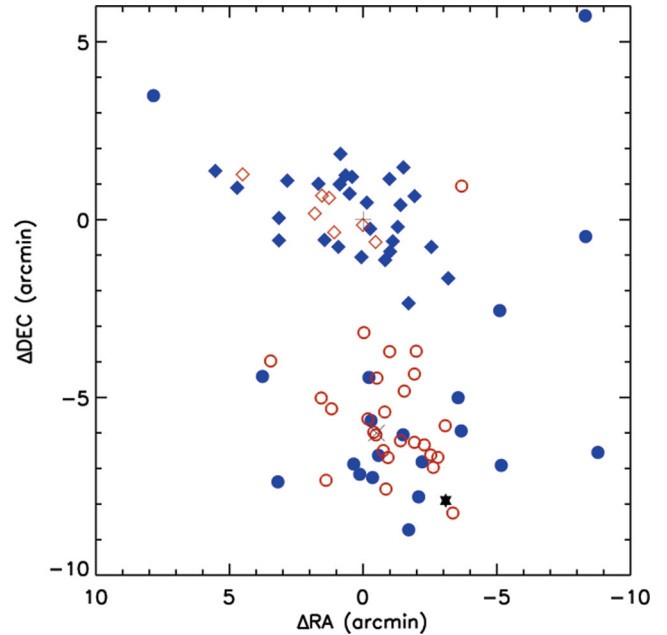


Figure 5. GC subpopulations for the spectroscopically confirmed GC systems of NGC 3607 and NGC 3608. The centres of NGC 3605, NGC 3607 and NGC 3608 are denoted with star ($-3.1, -7.9$), cross ($-1.1, -5.8$) and plus ($0, 0$) symbols. The diamonds and circles (both open and filled) represent, respectively, the GCs of NGC 3608 and NGC 3607. The red and blue colours represent the blue and the red subpopulations for both galaxies.

9 km s^{-1} from the galaxy stars, respectively, for NGC 3607 and NGC 3608.

4.3.1 GC subpopulations

Currently, we have 46 and 35 spectroscopically confirmed GCs, respectively, for NGC 3607 and NGC 3608. We have classified the GCs into blue and red subpopulations based on a constant colour division with galactocentric radius due to small number statistics. The Gaussian mixture modelling (GMM) algorithm (explained in Section 5.1.2) gives a ($g - i$) dividing colour of 0.87 for NGC 3607 and 0.93 mag for NGC 3608 (from photometric measurements). We used these colours to separate the blue and the red subpopulations of the two galaxies as shown in Fig. 5. From the photometric analysis of the GC subpopulations, we obtained 62 and 38 per cent blue and red subpopulations (see Section 5.2.2), respectively.

5 ANALYSIS OF PHOTOMETRIC DATA

Below we describe the radial density, colour and azimuthal distributions of the NGC 3607 and NGC 3608 GC systems. Note here that the GC systems are selected from the colour-colour space discussed in Section 3.

5.1 GC system of NGC 3607

5.1.1 Radial density distribution

To derive the radial distribution of the GC system, we define radial bins up to a galactocentric radius of 16.9 arcmin. Then the effective area coverage is obtained for each radial annulus. The area is corrected for the presence of saturated stars and for any regions outside the detection area. The GC number in each annulus is then

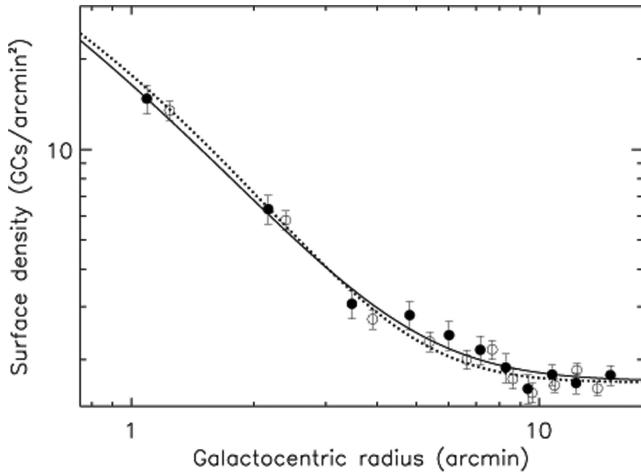


Figure 6. Surface density distribution for the GC system of NGC 3607. The GCs are selected via the SB and the MA methods shown by filled and open circles. The solid and the dotted lines represent the Sérsic fits for the GCs selected from each method. The GC system reaches the background around a galactocentric radius of 9.5 ± 0.6 arcmin, in agreement with the expected value using the galaxy stellar mass in the relation of Kartha et al. (2014).

Table 2. Fitted parameters for the surface density profile of the NGC 3607 GC system. The first column represents the method used for deriving the surface density profile. The effective radius, the Sérsic index and the background estimation are given in the following three columns. The last column presents the extent of the GC system as measured. The error values given are 1σ uncertainties.

Method	R_e (arcmin)	n	bg (arcmin $^{-2}$)	GCS ext. (arcmin)
SB	2.45 ± 0.54	2.74 ± 1.76	1.70 ± 0.15	9.4 ± 0.6
MA	1.99 ± 0.29	1.97 ± 1.19	1.68 ± 0.08	9.6 ± 0.5

divided by the effective spatial area to determine the spatial density in that particular annulus. The errors are calculated using Poisson statistics.

We obtained the GC system surface density using two methods. In the SB method (refer to Section 4.1), a correction is applied for the missing area due to NGC 3608 and NGC 3605. In the MA method (refer to Section 4.2), the number density is doubled in each radial bin. The radial density distribution is fitted with a combination of Sérsic profile plus a background parameter to estimate the effective radius and the background value for the GC system. The fitted surface density profile is

$$N(R) = N_e \exp \left[-b_n \left(\frac{R}{R_e} \right)^{\frac{1}{n}} - 1 \right] + bg, \quad (1)$$

where N_e is the surface density of the GCs at the effective radius R_e , n is Sérsic index or the shape parameter for the profile, b_n is given by the term $1.9992n - 0.3271$ and bg represents the background parameter. Note that the radius R is the centre of each radial bin.

Fig. 6 shows the density profile of the GC system for NGC 3607 only. The GCs brighter than the turnover magnitude, $i = 23.5$, only are considered. The plot displays the density values derived from the two different methods, i.e. SB and MA methods. Both are fitted with the profile given in equation (1). Table 2 tabulates the fitted parameters extracted from the radial density profile of NGC 3607, the SB and MA methods used 1170 and 907 objects, respectively. It

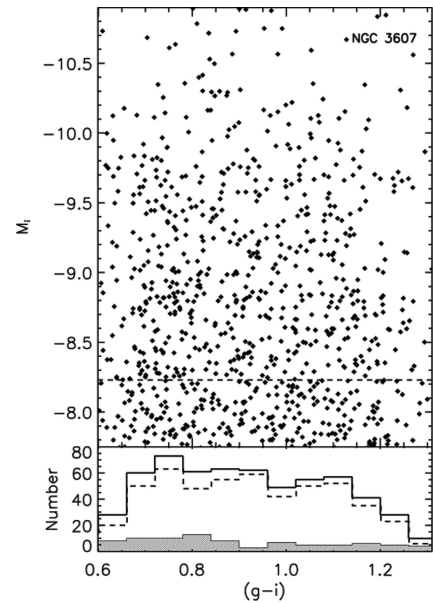


Figure 7. Colour–magnitude diagram for NGC 3607. The top panel represents the GCs brighter than $M_i = -7.75$ mag (0.5 fainter than the turnover magnitude) within the extent of NGC 3607 GC system. The dashed line represents the turnover magnitude in i filter, $M_i = -8.23$ mag. The bottom panel represents the colour histogram of NGC 3607 GC system. The solid, shaded and dashed histograms represent the GCs which are brighter than the turnover magnitude, the estimated background contamination and the background-corrected colour histograms.

is evident from the figure that both methods yield consistent results and the profile reaches the background at a galactocentric radius of 9.5 ± 0.6 arcmin (61 ± 3 kpc).

Kartha et al. (2014) found an empirical relation between the galaxy stellar mass and the extent of its GC system. The relation is as follows:

$$\text{GCS extent (kpc)} = [(70.9 \pm 11.2) \times \log(M/M_\odot)] - (762 \pm 127). \quad (2)$$

NGC 3607, an S0 galaxy, with absolute V -band magnitude $M_V^T = -21.87$ and assumed M/L ratio of 7.6 (given in Zepf & Ashman 1993) has a host galaxy mass, $\log(M/M_\odot) = 11.56$. The GC system extent for NGC 3607 determined using the above equation is 57 ± 3 kpc, in good agreement with the direct estimation using the wide-field Subaru/Suprime-Cam image (61 ± 3 kpc).

5.1.2 GC bimodality

Fig. 7 shows the colour–magnitude diagram of NGC 3607 GCs. The GCs, brighter than $M_i = -7.75$ mag, within the GC system extent of NGC 3607 are shown in the diagram. The bottom panel contains the histogram of GCs which are brighter than the turnover magnitude ($M_i = -8.23$ mag) along with the background contamination. To estimate the background contamination, we made use of the detected objects beyond the GC system extent of the galaxy. For NGC 3607, the objects beyond 11 arcmin (as GC system extent is 9.5 ± 0.6 arcmin) are considered as background contamination. We applied an areal correction, if needed. The background-corrected colour histogram is also shown in Fig. 7 and it includes 611 GCs.

To quantify the colour distribution of the GC system, we used the GMM (Muratov & Gnedin 2010; Li & Gnedin 2014) algorithm

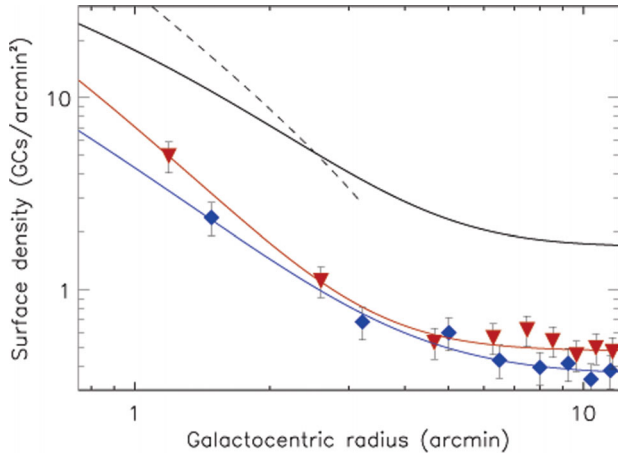


Figure 8. Radial density distributions of GC subpopulations for NGC 3607. The density distributions for the blue and the red subpopulations (from the MA method) are represented with blue diamonds and red triangles, respectively. The best-fitting Sérsic profiles to the density distributions are shown as solid lines. The black solid line represents the best-fitting Sérsic profile for the total GC system. The dashed line represents the galaxy brightness profile in the i filter. The blue subpopulation is found to be more extended than the red subpopulation. However, the galaxy stellar light profile better matches with the density distribution of the red subpopulation than the blue subpopulation.

Table 3. Fitted parameters for the surface density profile of NGC 3607 and NGC 3608 GC subpopulations. The first and second columns represent the target galaxy and subpopulation category. The derived parameters, effective radius, the Sérsic index and the background estimation, after the Sérsic fit are given in the last three columns.

NGC	GC	R_e (arcmin)	n	bg (arcmin $^{-2}$)
3607	Blue	1.59 ± 0.94	4.14 ± 2.32	0.36 ± 0.12
	Red	0.67 ± 0.52	3.38 ± 1.35	0.48 ± 0.05
3608	Blue	1.42 ± 0.31	1.03 ± 0.89	0.50 ± 0.05
	Red	0.91 ± 0.72	1.98 ± 0.82	0.35 ± 0.05

on the GC system ($g - i$) colour, after background correction. The algorithm tests for a multimodal colour distribution over unimodal. To be a significant multimodal GC system distribution, the following three statistics should be followed: (1) low values for the confidence level from the parametric bootstrap method, (2) the separation (D) between the means and the respective widths greater than 2, and (3) negative kurtosis for the input distribution.

For NGC 3607, the GMM algorithm confirmed a bimodal colour distribution from the SB and MA method selected GCs, based on the following statistics: with less than 0.001 per cent confidence level, $D > 2.6 \pm 0.3$ and negative kurtosis. The blue and red GC subpopulations peak in ($g - i$) colour at 0.74 ± 0.04 and 1.03 ± 0.03 , respectively. The ($g - i$) colour of separation between the blue and the red subpopulations is at 0.87 ± 0.02 . The total GC system is classified into 45 ± 9 and 55 ± 8 per cent, respectively, blue and red subpopulations.

The radial density distributions for both GC subpopulations (from the MA method) are estimated and plotted in Fig. 8. Both subpopulation distributions are fitted with Sérsic profile given in equation (1). The parameters derived from the Sérsic fit are tabulated in Table 3. The red subpopulation is centrally concentrated, while the blue subpopulation is more extended. The red subpopulation ap-

pears to have higher number density for most galactocentric radii. The galaxy stellar light profile is in better agreement with the density distribution of red subpopulation than blue subpopulation. Also the effective radius of the galaxy stellar light (39 arcsec) matches more with the red subpopulation (40 ± 29 arcsec) than the blue ones (95 ± 50 arcsec).

5.1.3 Azimuthal distribution

To quantify the azimuthal distribution of GCs, they are initially folded along the north–south direction, then binned in equal angular intervals. The azimuthal distribution, $\sigma(R, \theta)$, is then fitted with a profile (McLaughlin, Harris & Hanes 1994) of the form

$$\sigma(R, \theta) = kR^{-\alpha} [\cos^2(\theta - \text{PA}) + (1 - \epsilon^2)^{-2} \sin^2(\theta - \text{PA})]^{-\alpha/2} + bg, \quad (3)$$

where α is the power-law index fitted to the surface density of GCs, bg is the background estimated from the Sérsic fits (see Section 5.1.1) and k is the normalization constant. The profile is iterated with the position angle of the GC system (PA) and the ellipticity (ϵ) as free parameters. For the analysis, only the GCs within the extent of GC system (i.e. 9.5 arcmin) are included. The number of GCs in each angular bin is corrected for the missing area due to NGC 3608 in the SB method, and is doubled in the MA method. Here we used 980 and 564 GCs, respectively, in the SB and MA methods.

Fig. 9(a) shows the azimuthal distribution of GCs selected based on the SB method. The GCs are aligned to a position angle of 110 ± 7 deg, which is in reasonable agreement with the stellar light (125 deg) of the galaxy. The alignment of GC system is more elliptical (0.39 ± 0.08) than the stars (0.13). The GCs also show an enhancement along the minor axis (35 deg), which is either a genuine feature or possibly a contamination from the GCs of NGC 3608 and NGC 3605 (both positioned around the minor axis of NGC 3607). We already found a constant surface density around NGC 3605, and hence we assume that NGC 3605 is not contributing to the overabundance.

The only other possible contributor for this minor axis overabundance is NGC 3608, situated in the NE direction. We have eliminated the maximum contamination from NGC 3608 in the MA method, as it counts only the hemisphere away from the other galaxy. Hence, if the enhancement of GCs is not genuine, then we should not observe the same in the MA method. Fig. 9(b) displays the azimuthal distribution of GCs selected in the MA method, including only the GCs from 125 to 305 deg counted from north in anticlockwise direction. It is evident from this plot that the enhancement along the minor axis is a genuine feature, with decreased strength which is consistent within error bars. The position angle of GCs from the MA method also aligns with the galaxy stellar light. Similarly, from the SB method, the GCs are found to be more elongated than the arrangement of stellar light. Table 4 summarizes the best-fitting sinusoidal profile parameters.

Fig. 9 also shows the azimuthal distribution of blue and red GC subpopulations from the two methods. The subpopulations are separated at a ($g - i$) colour of 0.87 , obtained from the GMM algorithm. Both subpopulations have similar position angles for the total GC system and are more elliptical than the galaxy stars.

Summarizing, the total GC system and both subpopulations follow the galaxy stellar light in position angle. But the distribution of GCs is not as circular as the galaxy stellar component. The red GC subpopulation shows a more flattened distribution than the blue subpopulation for NGC 3607.

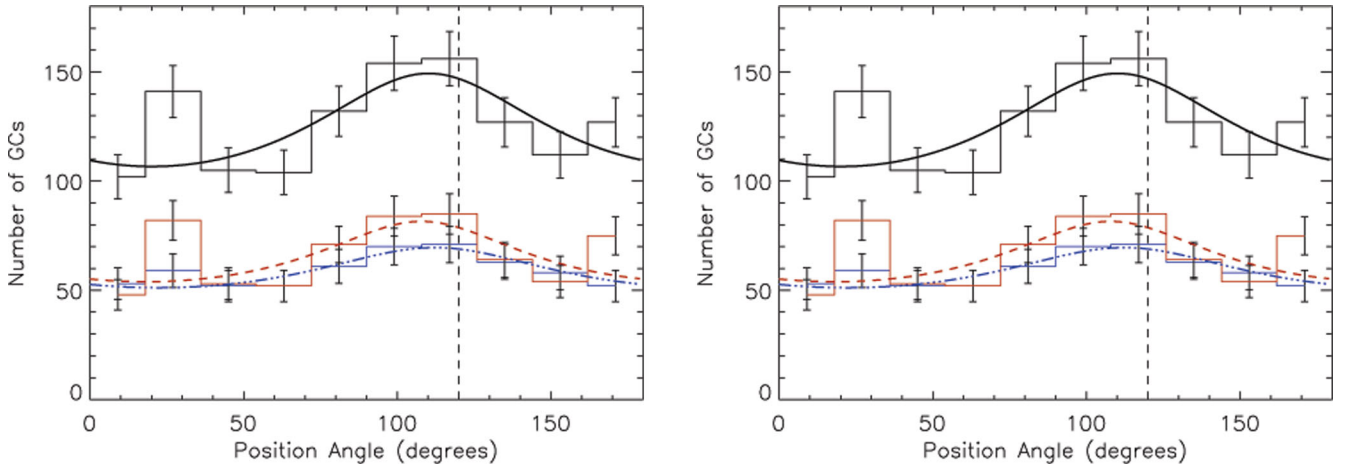


Figure 9. Azimuthal distribution for the GC system of NGC 3607. The black, blue and red histograms represent the azimuthal distribution of the total population and the blue and red subpopulations of GCs. The solid, dashed and triple-dot-dashed lines represent the fitted profiles based on equation (3). The vertical dashed line shows the position angle of the stellar major axis, 125 deg. The left-hand panel includes GCs selected on the basis of the SB method, whereas the right-hand panel includes GCs based on the MA method. In both panels, the total GC system and the blue and red subpopulations are aligned in a position angle which is in good agreement with the stellar light. An overabundance of GCs (majority from the red subpopulation) along the minor axis (35 deg) is seen in both panels.

Table 4. Position angle and ellipticity for the GC systems of NGC 3607 and NGC 3608. The values are derived by fitting equation (3) to the azimuthal distribution. The table gives the derived values for the total GC system, the blue and the red subpopulations. For comparison, the position angle and the ellipticity of the galaxy stellar light for NGC 3607 are 125 deg and 0.13, respectively, and for NGC 3608 are 82 deg and 0.20, respectively.

Method	GC	NGC 3607		NGC 3608	
		PA (°)	ϵ	PA (°)	ϵ
SB	Total	110 ± 7	0.39 ± 0.09	104 ± 15	0.20 ± 0.09
	Blue	112 ± 14	0.37 ± 0.11	106 ± 11	0.31 ± 0.10
	Red	108 ± 11	0.47 ± 0.09	97 ± 18	0.14 ± 0.16
MA	Total	109 ± 8	0.42 ± 0.07	66 ± 7	0.39 ± 0.10
	Blue	108 ± 10	0.45 ± 0.11	67 ± 8	0.45 ± 0.09
	Red	109 ± 8	0.48 ± 0.11	64 ± 10	0.44 ± 0.13

5.1.4 Radial colour distribution

Fig. 10 shows the radial distribution of GC colours from the centre of NGC 3607. The GCs brighter than the turnover magnitude in the MA method only are included. The GC subpopulations are divided with a moving colour with radius technique. In each radial bin, the average colours for both subpopulations are determined (keeping a constant number of GCs per radial bin). For NGC 3607, we used ~ 350 GCs to plot the colour distribution with 45 GCs in each bin.

As seen from the plot, for the total extent of the GC system, the average colour for the blue subpopulation decreases with radius from the centre, while a flat colour gradient is seen for the red subpopulation. The colour distribution for the blue subpopulation is fitted with a logarithmic relation (following Forbes et al. 2011) as

$$(g - i) = a + b \times \log(R/R_e), \quad (4)$$

where R_e is the effective radius for NGC 3607 equal to 39 arcsec (Brodie et al. 2014), a and b are, respectively, intercept and slope of the fit. We obtained a best-fitting line using the bootstrap technique and derived the parameters for the blue subpopulation as $a = 0.82 \pm 0.018$ and $b = -0.036 \pm 0.009 \text{ mag dex}^{-1}$. Maraston (2005)

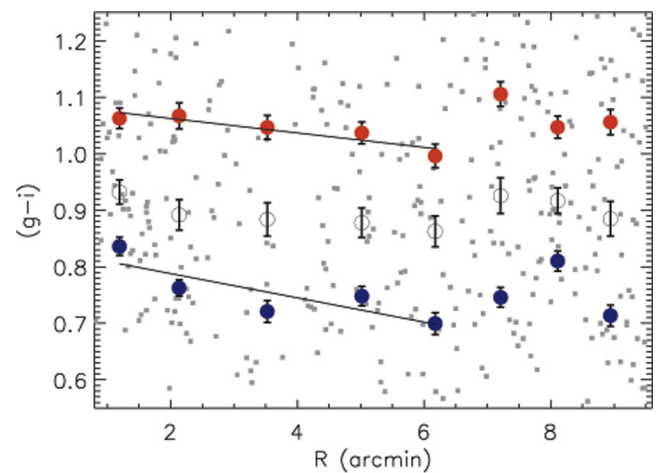


Figure 10. Radial colour distribution for the GC system of NGC 3607. The GCs are selected using the MA method, and are shown as small grey squares. The separation between the two subpopulations is obtained using a moving mean colour, and shown as black open circles. The average colours with errors for the blue and the red GC subpopulations are shown as blue and red filled circles, respectively. The solid lines represent the best-fitting lines for the blue and the red subpopulations in the central 6.5 arcmin, the projected separation between the two galaxies. For the blue and the red GC subpopulations, significant colour gradients (-0.070 ± 0.013 and $-0.033 \pm 0.015 \text{ mag dex}^{-1}$ for blue and red GC, respectively) are obtained in the central 6.5 arcmin radius.

derived a relation between $(g - i)$ and $[Z/H]$ over the metallicity range $[Z/H] \leq -0.2$, using single stellar population models, of $\Delta(g - i)/\Delta[Z/H] = 0.21 \pm 0.05 \text{ mag dex}^{-1}$. Using this we obtained for the blue subpopulation a metallicity gradient of $-0.17 \pm 0.04 \text{ dex dex}^{-1}$ to the total extent of the GC system. But, we did not detect a significant colour gradient for the red subpopulation and the total population in the total extent of GC system (-0.01 ± 0.01 and $-0.013 \pm 0.011 \text{ mag dex}^{-1}$ for red and total GCs).

We also quantified the colour/metallicity gradient in the central (~ 6.5 arcmin) region, only including the common galactocentric radii between the two galaxies. The colour gradients for the blue,

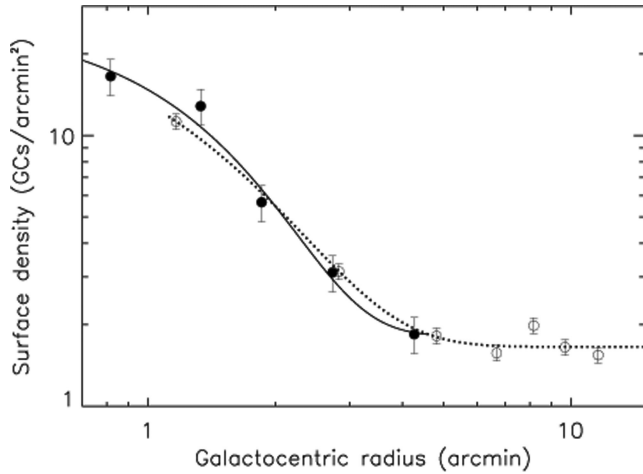


Figure 11. Surface density distribution for the GC system of NGC 3608. The radial density distributions of GCs based on the SB method and the MA method are represented with filled and open circles, respectively. The SB method detects GCs to a maximum galactocentric radius of ~ 5.5 arcmin. The best-fitting Sérsic profiles are represented with solid and dotted lines for the two methods. The GC system reaches a background in the MA method at a galactocentric radius of 6.6 ± 0.8 arcmin.

Table 5. Fitted parameters for the surface density of NGC 3608 GC system. The first column represents the GC selection method. The following three columns give the derived values for the effective radius, the Sérsic index and background using the Sérsic fit. The extent of the GC system is given in the last column, which is not estimated for the SB method.

Method	R_e (arcmin)	n	b_g (arcmin $^{-2}$)	GCS ext. (arcmin)
SB	1.29 ± 0.15	0.66 ± 0.36	1.82 ± 0.36	–
MA	1.50 ± 0.15	0.93 ± 0.56	1.65 ± 0.10	6.6 ± 0.8

red and the total population are -0.070 ± 0.013 , -0.033 ± 0.015 and -0.039 ± 0.018 mag dex $^{-1}$. In the inner 6.5 arcmin region, the blue subpopulation has a higher metallicity gradient (-0.33 ± 0.06 dex dex $^{-1}$) compared to the red subpopulation (-0.16 ± 0.07 dex dex $^{-1}$). Hence, we conclude that a significant colour/metallicity gradient is obtained for the blue and the red subpopulations of NGC 3607.

5.2 GC system of NGC 3608

5.2.1 Radial density distribution

Fig. 11 displays the radial density of GCs selected with the SB and the MA methods for NGC 3608 fitted with the profile given in equation (1) (fitted parameters are given in Table 5). In the SB method, the selection of GCs for NGC 3608 gives a maximum galactocentric radius of ~ 5.5 arcmin (as seen from Section 4.1). But the MA method identifies objects to a distance of 12.8 arcmin from the galaxy centre (thus extends up to the edge of the detection area). In both methods, the GCs with $i < 23.5$ mag (turnover magnitude) are counted for studying this distribution. In the density distribution plot, the SB and MA methods used 304 and 402 objects, respectively. The density distributions of GCs in radial annuli, after applying respective corrections for both methods, are shown in Fig. 11. The GC system reaches a background level of 1.65 ± 0.1 GCs per arcmin 2 to a galactocentric radius of 6.6 ± 0.8 arcmin (43 ± 5 kpc), from the MA method. But the density value for the

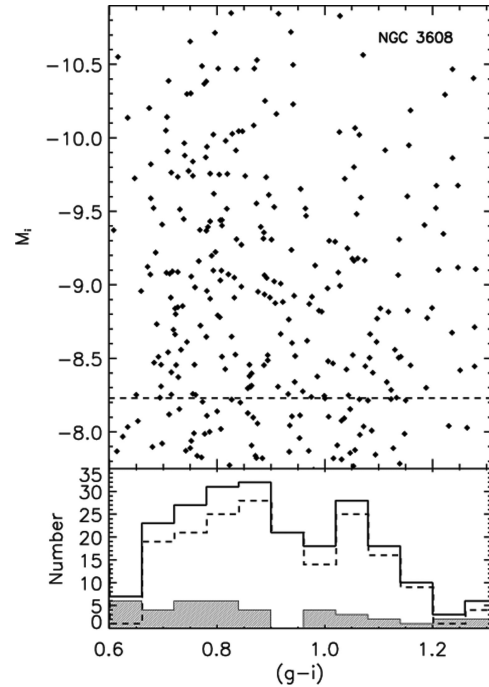


Figure 12. Colour–magnitude diagram for NGC 3608. The top panel represents the GCs brighter than $M_i = -7.75$ mag within the extent of GC system. The dashed line represents the turnover magnitude in i filter, $M_i = -8.23$ mag. The colour histogram of the GC system of NGC 3608 is shown in the bottom panel, where the solid, shaded and dashed histograms represent the GCs which are brighter than the turnover magnitude, the estimated background contamination and the background-corrected colour histograms.

final data point from the SB method is 1.82 ± 0.36 GCs per arcmin 2 implying that the distribution has not reached the background level. The elimination of marginal GCs (SB probability between 50 and 55 per cent) in the SB method might be the reason for this discrepancy in the extent of GC system. Another point from the figure is that the surface density values estimated from both methods are consistent within error bars, up to 5.5 arcmin.

NGC 3608, an E2 galaxy, with $M_V^T = -20.98$ mag and assumed M/L ratio of 10 (Zepf & Ashman 1993) has a stellar mass of log (M/M_\odot) = 11.32. Using equation (2), the expected GC system extent is calculated to be 40 ± 2 kpc, consistent with the GC system extent from the observational data (43 ± 5 kpc).

5.2.2 GC bimodality

The colour–magnitude diagram for the selected GCs of NGC 3608, within the GC system extent (43 kpc) and brighter than $M_i = -7.75$ mag, is shown in Fig. 12. The figure displays ~ 250 GCs. The background contamination in the GC system selection is quantified, as explained in Section 5.1.2, and the GC systems are corrected for this contamination. The bottom-right panel displays the colour histograms of GCs which are brighter than the turnover magnitude with and without background correction. The estimated background correction is also illustrated in the same figure.

The GMM algorithm fit to NGC 3608 GCs selected from the MA method gives a bimodal colour distribution with peaks at $(g - i) = 0.80 \pm 0.02$ and 1.12 ± 0.04 . The total GC system contains 65 ± 6 and 35 ± 6 per cent, respectively, blue and red subpopulations. The blue and red subpopulations are divided at $(g - i) = 0.93$.

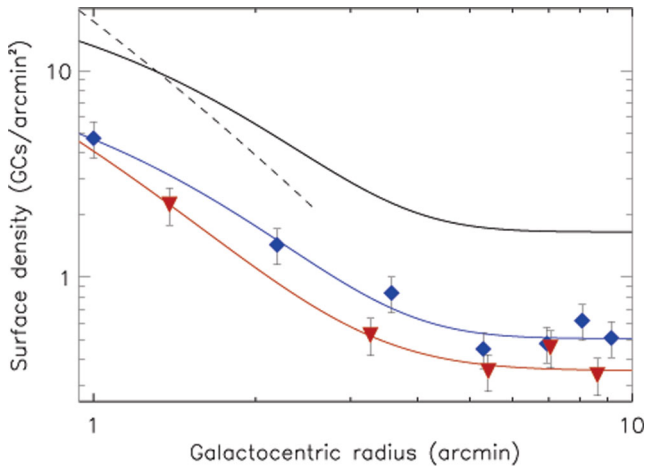


Figure 13. Radial density distributions of NGC 3608 GC subpopulations. The blue diamonds and the red triangles represent the surface density distributions of blue and red subpopulations, respectively. The blue and the red solid lines demonstrate the best-fitting Sérsic profiles on the distributions, while the black solid line represents the Sérsic fit for the total GC system. The galaxy brightness profile in the i filter is shown as a dashed line, in reasonable agreement with the density distribution of red subpopulation. Also, the red subpopulation is more centrally concentrated than the blue subpopulation for NGC 3608.

The radial surface densities (GCs from the MA method) are fitted with Sérsic profiles and are displayed in Fig. 13. The parameters estimated from the Sérsic fit are tabulated in Table 3. For NGC 3608, the blue subpopulation shows a higher density than the red subpopulation throughout the extent of the GC system. The red subpopulation is found to be more centrally concentrated, and their density profile is in good agreement with the galaxy stellar light.

5.2.3 Azimuthal distribution

The range of galactocentric radii for the selected GCs in the SB method is from 0.5 to 5.5 arcmin. The selection of GCs in all

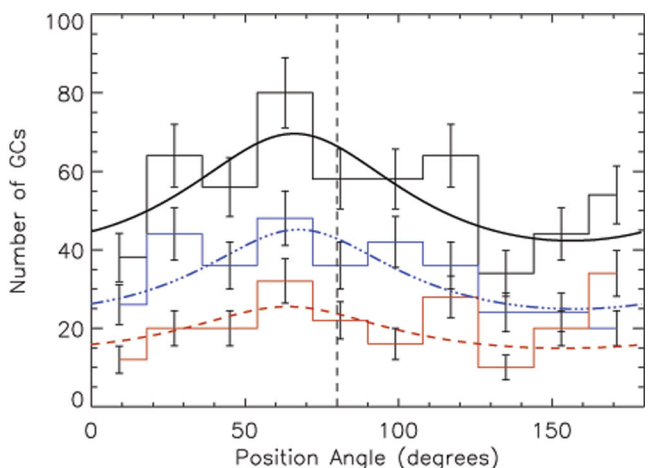
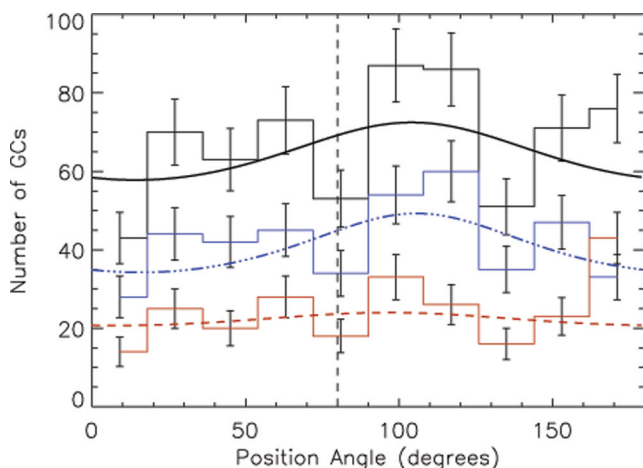


Figure 14. Azimuthal distribution for the GC system of NGC 3608. The colours and styles of histograms and lines are same as shown in Fig. 9. The left-hand panel shows the distribution of GCs selected from the SB method and the right-hand panel shows the distribution from the MA method. The galaxy stellar light is aligned along the major axis (82 deg), represented by the vertical dashed line. The total GC system and both the subpopulations are arranged along a different position angle (~ 100 deg) than the galaxy stellar light in the SB method. The right-hand panel shows the distribution of GCs selected from the MA method. The total GC system and both the subpopulations are aligned at a position angle, ~ 65 deg in the MA method, slightly off from the galaxy stellar light. Also in both panels, a scarcity of GCs along the galaxy major axis is visible.

position angles is complete up to 2.2 arcmin, and hence an areal correction is applied for the missing area outside that radius. Here we used 378 and 275 GCs, respectively, in the SB and MA methods. Fig. 14(a) shows the azimuthal density distribution of GCs from the SB method. The histograms are fitted with the sinusoidal profile given in equation (3). Table 4 gives the position angles and ellipticities obtained from the sinusoidal fit. The galaxy stellar light has a major axis of 82 deg and ellipticity of 0.20. As seen from Table 4, the total GC system and both subpopulations are arranged along a different position angle of ~ 100 deg for the SB method. When the distribution is examined over 0 to 360 deg rather than 0 to 180 deg (i.e. without folding along the north–south direction), an overabundance is evident in the position angles between 90 and 230 deg. This is in the direction towards NGC 3607 and also the direction in which the area correction is largest. Hence, this overabundance is either due to contamination from NGC 3607 (or due to overestimation of missing area). Also a scarcity of GCs is observed in both major axis position angles (82 and 262 deg). The ellipticity for the total GC system is 0.20 ± 0.09 , matching with the galaxy stellar light.

Fig. 14(b) shows the azimuthal density distribution of GCs selected in the MA method, for which GCs in the position angles 80 to 260 deg are underabundant. The GCs within the extent of GC system (6.6 arcmin) are included in the azimuthal distribution. As seen in Table 4, the best-fitting sinusoidal profile gives a position angle of 66 ± 7 deg for the total GC system and an ellipticity of 0.39 ± 0.10 . The GCs selected in the MA method include GCs of NGC 3608 placed at a position angle pointing away from NGC 3607, implying minimum contamination. The arrangement of GCs in the MA method is along the position angle matching the galaxy stars, but the distribution is more elliptical. Since we observed an overabundance in GCs for both galaxies, in the region towards each other, an interaction may be occurring between the two.

The total GC system is separated into subpopulations at $(g - i) = 0.93$ (obtained from the GMM algorithm). Regarding the azimuthal distribution of GC subpopulations, both subpopulations are aligned along the position angle of the total GC system in the two methods. Also the ellipticity of both subpopulations matches with the total

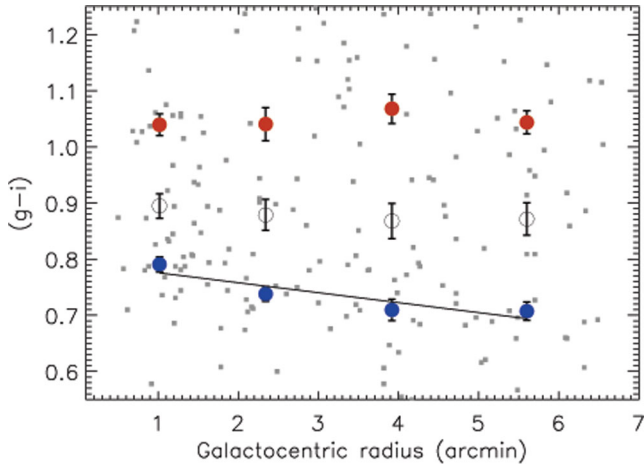


Figure 15. Radial colour distribution for the GC system of NGC 3608 (from the MA method). The individual GCs are represented as small grey squares. The average colours with error for the blue and red GC subpopulations are denoted as blue and red filled circles, respectively. The separation colours for the subpopulations in each radial bin are calculated using a moving mean colour method and are denoted with black open circles. The blue subpopulation shows a colour gradient of -0.052 ± 0.011 mag dex $^{-1}$ ($\Delta[Z/H] = -0.25 \pm 0.05$ dex dex $^{-1}$) for the total extent of the GC system, but we did not detect any colour gradient for the red subpopulation.

GC system. In the MA method, the total and both subpopulations are more elliptically aligned than the galaxy stellar light.

5.2.4 Radial colour distribution

Fig. 15 shows the radial ($g - i$) colour distribution of GC system of NGC 3608 selected on the MA method. To study this distribution, GCs (from the MA method) brighter than the turnover magnitude are selected, i.e. ~ 215 GCs. The total GC system and the red subpopulation show a null gradient, while the blue subpopulation shows a strong gradient along the total radial extent of the GC system. The colour distribution of the blue subpopulation is fitted with the logarithmic relation given in equation (4), where $R_e = 30$ arcsec (Brodie et al. 2014). The parameters, $a = 0.823 \pm 0.019$ mag and $b = -0.052 \pm 0.011$ mag dex $^{-1}$, are derived from the best-fitting profile using the bootstrap technique (shown in Fig. 15). The colour gradient, when converted to a metallicity gradient, gives $\Delta[Z/H] = -0.25 \pm 0.05$ dex dex $^{-1}$.

6 DISCUSSION

6.1 GC system distribution and galaxy effective radius

In this study of two group galaxies (NGC 3607 and NGC 3608 situated within a projected distance of 39 kpc), we introduce two methods, the surface brightness and the major axis methods, to separate the individual GC systems. For NGC 3607, the radial GC system extents determined from both methods are consistent with each other and in good agreement with the empirical relation for GC system extent (equation 2), initially presented in Kartha et al. (2014). From the radial surface density distribution, the red subpopulation is more centrally concentrated than the blue subpopulation. The galaxy surface brightness distribution is in agreement with the density distribution profile of the red subpopulation than the blue subpopulation (Fig. 8). Also, the effective radius of the galaxy stars (39 arcsec) is consistent with that of the red GC subpopulation

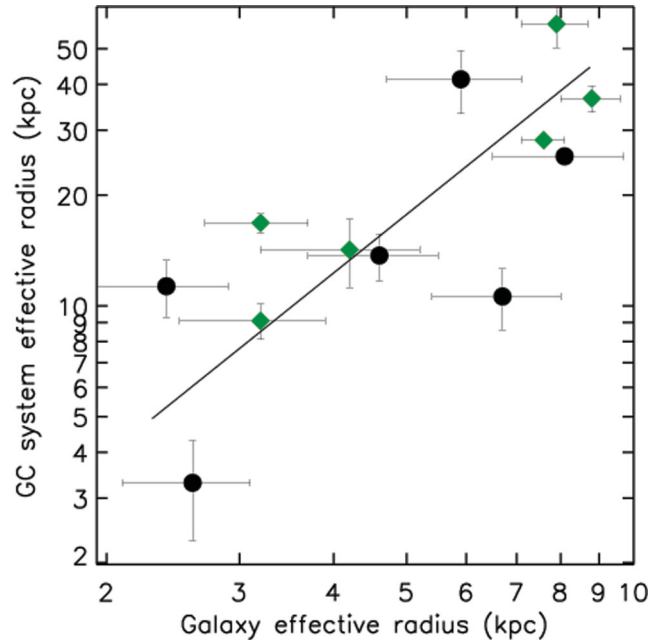


Figure 16. GC system effective radius versus galaxy effective radius. The plot displays NGC 3607, NGC 3608, NGC 4406, NGC 4472, NGC 4594 and NGC 5813 (represented by green diamonds) along with other six galaxies (black filled circles) from the earlier study of Kartha et al. (2014). The GC system effective radius is derived from the Sérsic profile fitted to the radial surface density distribution of GCs. The data in the plot are fitted with a linear relation using the bootstrap technique shown by a black line. The GC system effective radius is ~ 6 times the galaxy stellar light.

(40 ± 29 arcsec), while for the blue GC subpopulation it is 95 ± 50 arcsec. Both the spatial distribution and the effective radius measurements support the idea that the red GC subpopulation has evolutionary similarities with the galaxy stellar component (Forbes & Forte 2001; Larsen et al. 2001; Brodie & Strader 2006; Spitler 2010; Forbes et al. 2012).

For NGC 3608, the blue GC subpopulation is more extended than the red GC subpopulation. It is evident from Fig. 13 that the density distribution of the red GC subpopulation follows the galaxy stellar light distribution. However, the effective radius of galaxy light (30 arcsec) is half of the red subpopulation (59 ± 40 arcsec) and one third of the blue subpopulation (85 ± 18 arcsec). The effective radius of the red GC subpopulation is therefore not consistent with the stellar light component. Even so the resemblance of the density distribution profile with the galaxy stellar light might imply a significant association.

Fig. 16 displays the total GC system effective radius versus the galaxy effective radius and is an updated version (with the addition of six galaxies) of fig. 20 in Kartha et al. (2014). In this figure, the GC system effective radii are determined from Sérsic profile fits to the density distribution, which is currently available for 12 galaxies. The positions of the newly added galaxies, tabulated in Table 6, are compatible with the existing linear relation ($R_{e(\text{GCs})} = [(5.2 \pm 3.7) \times R_{e(\text{galaxy})}] - (8.5 \pm 6.5)$). The updated relation for the 12 galaxies is as follows:

$$R_{e(\text{GCs})} = [(6.5 \pm 1.3) \times R_{e(\text{galaxy})}] - (13 \pm 6), \quad (5)$$

where both R_e s are measured in kpc. When compared with the relation in Kartha et al. (2014), the above relation has a similar slope within error bars. The effective radii for both GC subpopulations are determined only for six galaxies. With the available data, we

Table 6. Effective radii for the GC systems and respective stellar surface brightness, from the two galaxies in this paper (NGC 3607 and NGC 3608) and other four galaxies. The last column provides the references for the GC system and galaxy effective radii, respectively.

Galaxy NGC	Effective radius		Ref.
	GC system (kpc)	Stellar light (kpc)	
3607	14.2 ± 2	4.2 ± 1	1, 2
3608	9.1 ± 1	3.2 ± 0.7	1, 2
4406	28.2 ± 1	7.6 ± 0.5	3, 4
4472	58.4 ± 8	7.9 ± 0.8	3, 4
4594	16.8 ± 1	3.2 ± 0.7	3, 4
5813	36.6 ± 3	8.8 ± 0.8	3, 4

References: 1 – This work; 2 – Brodie et al. (2014); 3 – Hargis & Rhode (2014); 4 – Cappellari et al. (2011).

could not detect any significant relation between the effective radius of GC subpopulations and the host galaxy stellar light.

From equation (5), we can infer that the GC system effective radius is ~ 6 times the galaxy effective radius, which confirms that the GC system of a galaxy extends further out than the bulk of its stellar component (Harris et al. 2000; Brodie & Strader 2006; Forbes et al. 2006b; Alamo-Martínez et al. 2012; Cantiello et al. 2015). A by-product from the above relation is that we can estimate the GC system effective radius by knowing the galaxy effective radius.

6.2 GC system ellipticity and galaxy ellipticity

To further address the association of galaxy stellar light with GC subpopulations, we need to study the two-dimensional spatial distribution of these systems. Different studies of two-dimensional distributions (position angle and ellipticity) have confirmed an association of both subpopulations with galaxy stellar light (e.g. NGC 2768 by Kartha et al. 2014, NGC 4636 by Dirsch, Schubert & Richtler 2005). Park & Lee (2013) analysed the two-dimensional shape parameters of 23 ETGs using the *HST*/ACSVCS. They found that the arrangement of both subpopulations is aligned with the photometric major axis of galaxies. Also, the red GC subpopulations show a tight relation in ellipticity with galaxy stellar light, while the blue GC subpopulations show a less tight relation. Concurrently, Kartha et al. (2014) obtained a similar relation for the red subpopulations from a sample of six galaxies using wide-field imaging.

Fig. 17 demonstrates the relation between GC subpopulation ellipticity and galaxy stellar light ellipticity for 10 ETGs. The plot is an updated version of fig. 22 in Kartha et al. (2014), with the addition of four galaxies (NGC 3607, NGC 3608, NGC 4406 and NGC 5813). Data for NGC 4406 and NGC 5813 are taken from Hargis & Rhode (2014). For NGC 4406, the stellar, blue and red subpopulation ellipticities are 0.4 ± 0.03 , 0.39 ± 0.06 and 0.36 ± 0.07 , respectively. Similarly, the ellipticities for stellar, blue and red GC subpopulations of NGC 5813 are 0.3 ± 0.03 , 0.52 ± 0.15 and 0.36 ± 0.11 , respectively. With the addition of four galaxies, we observe a tight one-to-one relation between red GC ellipticity and galaxy stellar light. The relation is

$$\epsilon_{\text{GC}} = [(1.0 \pm 0.1) \times \epsilon_{\text{Stars}}] + (-0.02 \pm 0.06). \quad (6)$$

The intrinsic scatter in the above relation is estimated to be 0.10. The one-to-one relation signifies that the red subpopulations are affiliated with the stellar light of the parent galaxies (Park & Lee 2013). In other words, both the red subpopulation and galaxy stellar

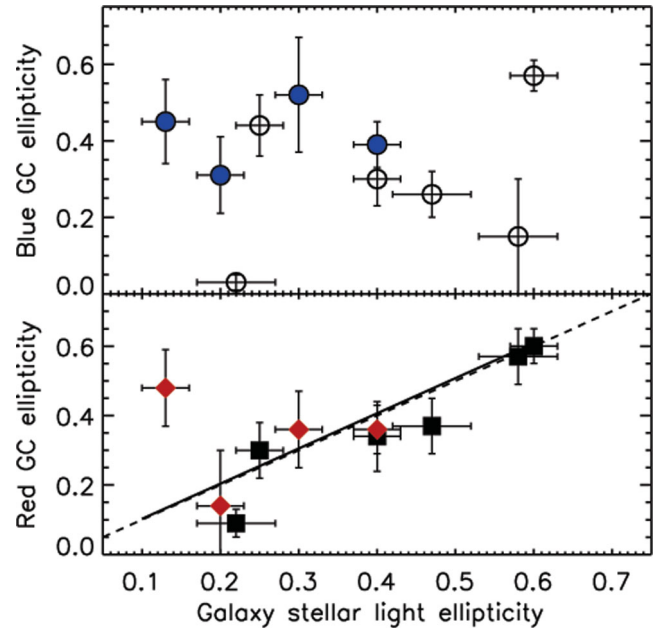


Figure 17. GC ellipticity versus galaxy stellar light ellipticity. The top and the bottom panels show the relation between ellipticities of blue GCs (open circles) and red GCs (filled diamonds) versus galaxy stellar light, respectively. Each panel includes an additional four galaxies (in red or blue colours) with the six galaxies (in black colour) from Kartha et al. (2014). A linear fit to the red GCs (red and black diamonds) is drawn as a solid line and a one-to-one relation is shown as a dashed line. The red GC subpopulation confirms a one-to-one relation with galaxy stellar light, whereas only a weak relation for the blue GC subpopulation is present.

light might have a similar origin. In contrast to Park & Lee (2013), we notice a poor association of blue GC subpopulation ellipticity with galaxy stellar light ellipticity. We explain this as a consequence of our wide-field imaging, as the ACSVCS data used by Park & Lee (2013) do not reach far out enough to detect the whole blue GC subpopulation for the most extended galaxies (Peng et al. 2006).

In this small sample of 10 galaxies, NGC 3607 shows the lowest ellipticity (nearly circular at $\epsilon = 0.13$) for the galaxy stellar component. For NGC 3607, the ellipticities of both GC subpopulations show a deviation from the galaxy stellar light, although both are arranged along the photometric major axis of the galaxy. So, NGC 3607 supports the idea that galaxies with low ellipticities might have randomly arranged GC subpopulations (Wang et al. 2013). The difference in spatial distribution of GC subpopulations from the galaxy stellar component suggests that a major fraction of both GC subpopulations might have formed separately from the galactic stars and later settled in the host galaxies. In the case of NGC 3608, both GC subpopulations show deviations from the galaxy stellar light in position angle. In addition, the blue GC subpopulation shows a more elongated distribution than the red GC subpopulation.

In addition to NGC 3608, three other galaxies – NGC 4365, NGC 4406 and NGC 5813 – also have blue GC subpopulations more elongated in shape than the red GC subpopulations. The elongated shape of the blue GC subpopulation suggests that it shows spatial distribution similarities with the red subpopulation that mostly follows the distribution of galaxy stellar component. If the distribution of blue GCs is not spherical, Wang et al. (2013) suggest that it may not have been built from accretions that were equally distributed in all directions. Instead, they might have formed through local filamentary structures in particular directions. This points out that

direction-dependent accretion or minor mergers might have occurred in these galaxies, altering the shape of blue GC subpopulations.

In addition, these four elliptical galaxies are all slow rotators with kinematically distinct cores (KDCs; Emsellem et al. 2011; Krajnović et al. 2011). Naab et al. (2014) carried out hydrodynamical simulations to kinematically study the centres of ETGs. They suggested that KDCs were generally formed in slow rotators that had experienced multiple gas-poor minor mergers. They proposed that their recent mass assembly histories are devoid of any major mergers and are expected to have older stellar populations. Few, if any GCs, are expected to have formed from such mergers. It is unclear whether blue GCs from the accreted galaxies would form a more elongated distribution than the host galaxy starlight as we observe.

In summary, the ellipticities of red GC subpopulations have a one-to-one relation with the galaxy stellar light ellipticities, whereas only a weak relation is seen for the blue GC subpopulation. Additionally, slowly rotating galaxies with a KDC have larger values for blue GC subpopulation ellipticities than their red GC counterparts. The elongated shape of the blue GC subpopulations may be due to recent minor mergers that were asymmetric in direction (Tempel et al. 2015).

6.3 GC metallicity gradients and galaxy stellar mass

Colour gradients are important observational features for exploring the formation history of GC subpopulations and are clues to galaxy mass assembly. A negative colour gradient (GCs are redder at the centre of the galaxy than the outskirts) represents either the presence of younger (or more metal-rich) GCs at the galaxy centre or older (more metal-poor) GCs at the outskirts. As GCs are observed to be mostly old (~ 10 Gyr; Strader et al. 2005; Dotter et al. 2010; Forbes et al. 2015), the colour gradients are basically caused by metallicity gradients rather than age gradients.

The observed gradients in GC subpopulations help discriminate between the different galaxy formation processes: e.g. a negative gradient is predicted when the GCs are formed from a dissipative collapse (Pipino et al. 2010), while a gas-poor major merger will wash away any existing gradient (Di Matteo et al. 2009), a gas-rich major merger may remake a new gradient different from the original one (Hopkins et al. 2009), etc. Also, minor mergers (accretions) can deposit GCs in the outskirts of galaxies (Hirschmann et al. 2015; Pastorello et al. 2015) which will alter the existing gradient, perhaps resulting in an inner negative gradient and a flat outer gradient (Oser et al. 2010; Forbes et al. 2011).

The first detection of a radial colour gradient in a GC system was performed by Geisler, Lee & Kim (1996) in NGC 4472. With ground-based data, GC colour gradients have been detected in other massive galaxies (NGC 4486: Harris 2009; NGC 1407: Forbes et al. 2011; NGC 4365: Blom et al. 2012), while only seen in a handful of intermediate-mass galaxies (NGC 3115: Arnold et al. 2011; NGC 4564: Hargis & Rhode 2014) to date.

In NGC 3607, another intermediate-mass galaxy, the mean colours of both the blue and the red GC subpopulations reveal a significant colour gradient in the inner 6.5 arcmin ($10 R_e$). The colour gradient for the blue subpopulation is steeper than the red subpopulation. Within the total extent of the GC system (beyond $10 R_e$), only the blue subpopulation has a significant colour gradient. We detect a significant colour gradient only for the blue GC subpopulation of NGC 3608.

Table 7. List of 12 galaxies observed with metallicity gradients for GC subpopulations. The metallicity gradients ($\Delta[Z/H]$) given below are obtained from the colour gradients. Galaxy name, logarithmic galaxy stellar mass, metallicity gradients for blue and red GC subpopulations with errors and the corresponding references (for colour gradient followed by the transformation equation used) are given.

Galaxy NGC	$\log(M_*)$ (M_\odot)	Metallicity gradient		Ref.
		Blue GCs (dex dex ⁻¹)	Red GCs (dex dex ⁻¹)	
1399	11.660	-0.12 ± 0.05	-0.10 ± 0.05	1, 14
1399	11.660	-0.21 ± 0.04	–	2, 11
1407	11.892	-0.22 ± 0.04	-0.24 ± 0.07	3, 10
3115	11.249	-0.17 ± 0.03	-0.24 ± 0.06	4, 10
3115	11.239	-0.27 ± 0.06	-0.11 ± 0.10	5, 5
3607	11.677	-0.33 ± 0.06	-0.16 ± 0.07	6, 10
3608	11.205	-0.25 ± 0.05	–	6, 10
3923	11.796	-0.18 ± 0.07	-0.17 ± 0.08	5, 5
4278	11.290	-0.23 ± 0.10	-0.23 ± 0.12	7, 14
4365	11.843	-0.19 ± 0.01	-0.22 ± 0.03	8, 14
4472	12.046	-0.08 ± 0.04	-0.10 ± 0.05	1, 14
4472	12.046	-0.13 ± 0.03	-0.10 ± 0.05	9, 11
4486	11.953	-0.12 ± 0.02	-0.12 ± 0.03	1, 14
4486	11.953	-0.09 ± 0.01	-0.12 ± 0.01	10, 10
4486	11.953	-0.17 ± 0.07	-0.17 ± 0.05	11, 11
4594	11.653	-0.17 ± 0.04	-0.17 ± 0.04	12, 12
4649	11.867	-0.00 ± 0.04	-0.05 ± 0.02	5, 5
4649	11.867	-0.21 ± 0.05	–	13, 14

References: 1 – Liu et al. (2011); 2 – Bassino et al. (2006b); 3 – Forbes et al. (2011); 4 – Arnold et al. (2011); 5 – Faifer et al. (2011); 6 – This paper; 7 – Usher et al. (2013); 8 – Blom et al. (2012); 9 – Geisler et al. (1996); 10 – Harris (2009); 11 – Forte, Vega & Faifer (2012); 12 – Hargis & Rhode (2014); 13 – Strader et al. (2012); 14 – Usher et al. (2013).

Table 7 compiles the list of galaxies in which colour gradients are detected for the GC subpopulations. The colour gradients are detected in different colour filters. For a uniform comparison, the different colour gradients are converted to metallicity gradients ($\Delta[Z/H]$) using colour–metallicity transformation equations (references are given in Table 7). The converted metallicity gradients are given in Table 7. The list includes the gradients obtained only from wide-field imaging data, and hence we exclude galaxies with single pointing *HST/ACS* imaging. This criterion excludes most galaxies from Liu et al. (2011), for which only the central regions of target galaxies were covered. The sample of galaxies in the table includes 2 galaxies from this paper plus another 10 galaxies. The galaxy stellar masses are also tabulated. In order to calculate the galaxy stellar masses, we used their distance and visual magnitude from NED and the M/L ratios of Zepf & Ashman (1993). In the sample of 12 galaxies, half have multiple measurements of their metallicity gradients. We include all measured GC gradients and their quoted uncertainties for the 12 galaxies. This comprises 18 measurements of blue GC gradients and 15 measurements of red GC gradients for 12 galaxies.

In Table 7, multiple measurements are given for five galaxies. For the same galaxy, the observed gradients are not always consistent among different works. For example, in the case of NGC 4649, the gradients for the blue subpopulation are -0.00 ± 0.04 (Faifer et al. 2011) and -0.21 ± 0.05 (Strader et al. 2011). Both studies extended to $7 R_e$. In another example, the gradient for the red subpopulation of NGC 3115 is quoted in Arnold et al. (2011) as -0.24 ± 0.06 , while Faifer et al. (2011) quoted -0.11 ± 0.1 . But in the case of NGC 4472, Geisler et al. (1996) and Liu et al. (2011) found consistent gradients for the red subpopulation.

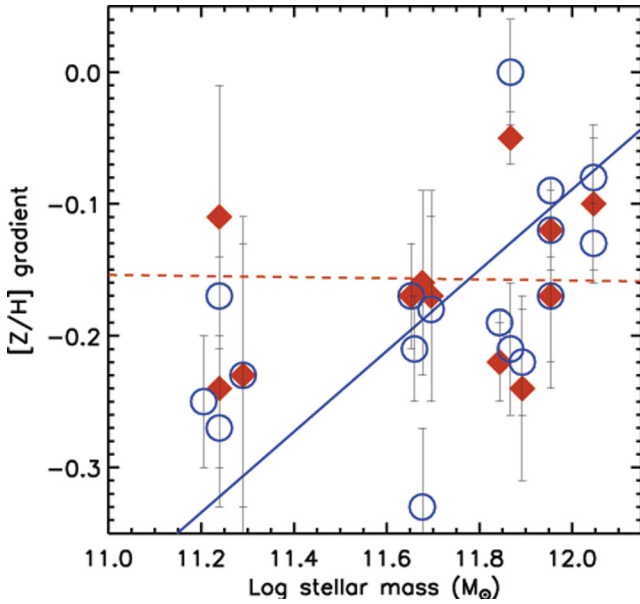


Figure 18. Metallicity gradients of GC subpopulations versus galaxy stellar mass. The metallicity gradients (converted from colour gradients) for the blue (blue open circles) and the red (red filled diamonds) GC subpopulations for 12 galaxies are plotted against host galaxy stellar mass. The blue solid line and the red dashed line represent the linear fits to the metallicity gradients of blue and red GCs, respectively. It is evident from the plot that for the blue GC subpopulation, the metallicity gradients become shallower with increasing galaxy stellar mass. Note that multiple measurements of metallicity gradients for the same galaxy are included.

Fig. 18 shows the metallicity gradients for blue/red GC subpopulations versus the galaxy stellar mass. We plot multiple measurements for individual galaxies. Linear fits are carried out separately for the blue and the red GCs with uncertainties estimated from the bootstrap technique. The technique uses the errors associated with individual gradients. Best-fitting relations are

$$\Delta[Z/H]_{\text{BGC}} = [(0.31 \pm 0.08) \times \log(M_*)] - (3.8 \pm 0.9) \quad (7)$$

$$\Delta[Z/H]_{\text{RGC}} = [(0.004 \pm 0.1) \times \log(M_*)] - (0.1 \pm 1.0). \quad (8)$$

The galaxies in our sample have a mass range $11.0 < \log(M_*) < 12.0 M_\odot$. From the above relations, we find that the metallicity gradient for the blue subpopulation has a significant correlation with stellar mass; the negative gradients flatten with increasing stellar mass. As more massive galaxies are expected to accrete more satellites (Oser et al. 2010), we expect more GC accretion to have taken place in these galaxies. This addition of mostly blue GCs at different galactocentric radii may make the initial gradient of the blue GCs shallower. In addition, Hirschmann et al. (2015) found that gradients resulting from major mergers are shallower in more massive galaxies due to radial mixing of GCs. From the spectroscopic metallicities of GC subpopulations in 12 ETGs, Pastorello et al. (2015) observe a similar trend of decreasing metallicity gradient with increasing galaxy stellar mass.

For the red GC subpopulation, we are unable to find a significant relation between the metallicity gradient and galaxy stellar mass. In comparison with the blue GC subpopulations, the metallicity gradients for the red GC subpopulations have higher errors and also a lower number of data points. In Table 7, the least significant gradient measurement is for the red subpopulation of NGC 3115

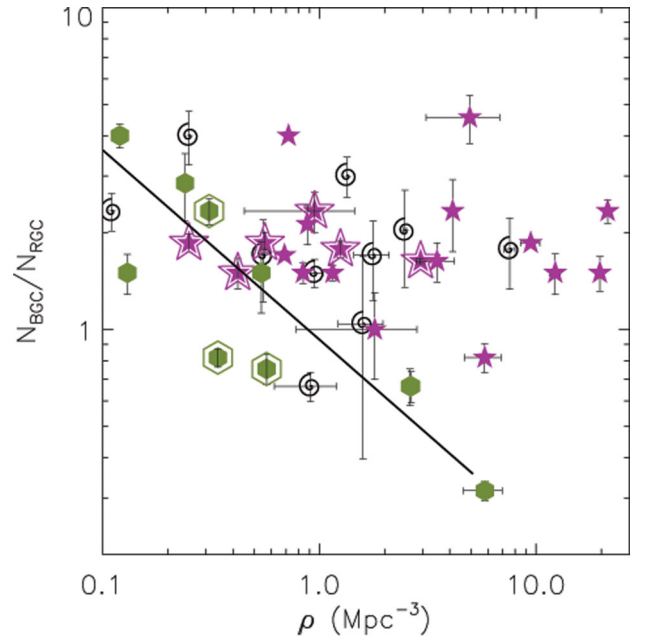


Figure 19. Ratio of blue to red GCs versus density of environment. Spirals, lenticular galaxies and elliptical galaxies are represented by spirals, hexagons and stars, respectively. The galaxies from the SLUGGS survey are shown as double symbols. This is an updated version of fig. 21 in Kartha et al. (2014) with the addition of NGC 3607 and NGC 3608. The position coordinates for NGC 3607 and NGC 3608 are, respectively, (0.34, 0.79) and (0.56, 1.85). NGC 3607 is consistent with the correlation shown by lenticular galaxies.

(Faifer et al. 2011). Hence, we carried out another fitting for the red GCs without that measurement and the best-fitting relation is

$$\Delta[Z/H]_{\text{RGC}} = [(0.07 \pm 0.05) \times \log(M_*)] - (0.95 \pm 0.86). \quad (9)$$

From the above relation, we infer that the gradients for the red GC subpopulation show a very weak dependence on galaxy stellar mass.

The galaxy stellar mass is derived from the M/L ratios that are given in Zepf & Ashman (1993). We appreciate that the Zepf & Ashman (1993) values are an approximation but have chosen to use them as this is the approach we took in Kartha et al. (2014), which follows from the same approach as used by Rhode, Windschitl & Young (2010) and Spitler et al. (2008). So in order to match the results with the above-mentioned publications, we use the same method. Bell et al. (2003) derived the relationships to estimate the stellar mass from galaxy colours (see Appendix B for details). We used their relationship to derive the galaxy stellar mass from $(B - V)$ colour. We find that equations (7)–(9) are statistically unchanged when using Bell et al. (2003) to derive galaxy stellar masses.

In summary, we suggest that the subsequent addition of GCs from minor mergers may weaken any pre-existing gradients in metallicity (from an early dissipative formation event) both for the blue and the red GC subpopulations.

6.4 Ratio of blue to red GCs with environment density and galaxy mass

Fig. 19 shows the ratio of blue to red GCs versus the environment density for a sample of 42 galaxies (2 from this paper and 40 from Kartha et al. 2014). We note that the blue-to-red GC ratio is largely insensitive to any GC magnitude incompleteness. With

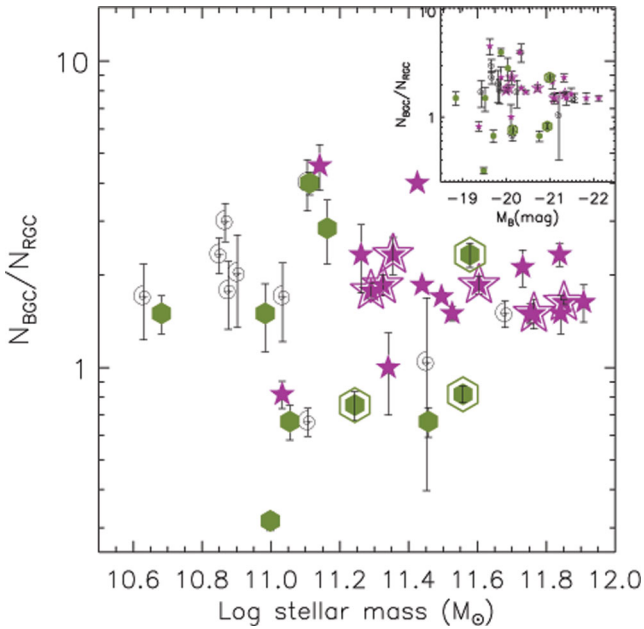


Figure 20. Ratio of blue to red GCs versus galaxy stellar mass. The representation of symbols is same as in Fig. 19. For all types of galaxies, there is no correlation between the ratio of blue to red GCs and galaxy stellar mass. They have a mean ratio of $N_{\text{BGC}}/N_{\text{RGC}} \sim 1.7$ for the total sample. An inset plot of ratio of blue to red GCs versus galaxy absolute B -band magnitude is given for the same sample. The mean ratio of blue to red GCs is ~ 1.7 for the galaxy range $-18.5 < M_B < -22$ mag.

this sample of galaxies, it is evident that neither spiral nor elliptical galaxies show any particular trend in the ratio of blue to red GCs with environment density. NGC 3608, with $N_{\text{BGC}}/N_{\text{RGC}} = 1.85$ and density = 0.56 Mpc^{-3} (Tully 1988), is consistent with the other elliptical galaxies.

Kartha et al. (2014) found that the fraction of blue to red GCs in lenticular galaxies decreases with local density of environment. This suggests that lenticular galaxies residing in high-density environments accommodate a higher fraction of red GCs. NGC 3607 is a lenticular galaxy with a relatively high fraction of red GCs ($N_{\text{BGC}}/N_{\text{RGC}} = 0.79$ and density = 0.34 Mpc^{-3} from Tully 1988). The position of NGC 3607 is consistent with the trend of decreasing fraction of blue to red GCs with increasing environment density.

In Fig. 20, the ratio of blue to red GCs is plotted against the host galaxy stellar mass for the above sample of 42 galaxies. There is no obvious correlation between the ratio of blue to red GCs with the galaxy stellar mass. We divide the galaxies into three mass bins of size $0.5 M_{\odot}$ and derive the mean value for the ratio of blue to red GCs. The mean ratio of blue to red GCs in the low- ($\log(M_*) < 11 M_{\odot}$), intermediate- ($11 < \log(M_*) < 11.5 M_{\odot}$) and high-mass ($\log(M_*) > 11.5 M_{\odot}$) bins are, respectively, 1.7 ± 0.8 , 2.0 ± 1.2 and 1.6 ± 0.4 . The mean ratio of blue to red GCs for the total sample of 42 galaxies is ~ 1.76 .

Using cosmological simulations, Bekki et al. (2008) investigated the structural, kinematical and chemical properties of GC systems in different Hubble-type galaxies. They estimated the ratio of blue to red GCs, in the host galaxy luminosity range $-14 < M_B < -22$, to vary from ~ 50 to 0.25 , with an average of 1.5 . Using the ACSVCS, Peng et al. (2006) also investigated the ratio of blue to red GCs in a similar luminosity range and determined that the fraction varies from 5.6 to 0.67 per cent from low- to high-luminosity galaxies,

suggesting an average ratio of ~ 1.5 blue to red GCs over the total luminosity range.

There is a decreasing trend in the ratio of blue to red GCs with host galaxy luminosity, both observationally (Peng et al. 2006) and theoretically (Bekki et al. 2008). We observe a nearly constant ratio of blue to red GCs in our sample of 42 galaxies because our luminosity range is much more restricted. As seen in the inset of Fig. 20, our sample of 42 galaxies lie in the galaxy luminosity range $-18.5 < M_B < -22$ mag, whereas the faint end extends to $M_B = -14$ mag for both Peng et al. (2006) and Bekki et al. (2008).

6.5 Formation of GC systems

6.5.1 NGC 3607 and NGC 3608

In the Leo II group, NGC 3607 is the massive central galaxy and has a red GC subpopulation fraction higher than the blue, while the neighbouring galaxy NGC 3608 is less massive and has a higher fraction of blue GCs. An overabundance of red GCs is observed along the minor axis of NGC 3607 (even after removing the GCs in the direction towards NGC 3608). From the azimuthal distribution of GCs of NGC 3608, it is found that both GC subpopulations are aligned in position angle and that angle is different from the position angle of the galaxy stellar light. These results (overabundance and misalignment) suggest a possible interaction between the galaxies in the group.

Using *HST* data, Lauer et al. (2005) carried out an imaging study of 77 ETGs, including NGC 3607. They detected an additional gas disc settling in NGC 3607 perpendicular to the existing dusty disc. They commented that the dusty disc is in a transition phase merging with the gas disc. They explained this process as gas infalling directly on to the centre of NGC 3607 without disturbing the dusty disc and without any obvious features of interaction.

Later, Annibali et al. (2007) studied the stellar population properties of 66 ETGs. They estimated the age, metallicity and alpha enhancement using the Lick indices with updated simple stellar population models (including the non-solar element abundance patterns). They estimated a very young age, 3.1 ± 0.5 Gyr, for NGC 3607 and suggested it had experienced a recent episode of star formation. Rickes et al. (2009) carried out long-slit spectroscopy, out to galactocentric radii of 30.5 arcsec, and claimed that NGC 3607 has undergone a minimum of three star formation episodes with ages ranging from 1 to 13 Gyr. The young age for the stellar population of NGC 3607 and the detection of a central gas disc indicate that NGC 3607 has experienced a recent star formation episode and the overabundance of red GCs may be due to GCs formed in that episode.

From the ATLAS^{3D} survey, McDermid et al. (2015) estimated the mass-weighted ages for NGC 3605, NGC 3607 and NGC 3608 to be 8.1 ± 0.8 , 13.5 ± 0.7 and 13.0 ± 0.7 Gyr, respectively. They utilized the spectra within $1 R_e$ to fit the single stellar population models and hence derive the mass-weighted ages, metallicity and star formation histories of 260 ETGs. Using the Lick indices, they estimated the age for NGC 3607 to be 7.3 ± 1.3 Gyr that contradicts the young age determined by Annibali et al. (2007).

Forbes et al. (2006a) carried out a multiwavelength (X-ray, optical and H I imaging) study of ~ 60 galaxy groups, including the Leo II group. They investigated the evolutionary connections between different groups and the influence of group environment. In their study, they detected extended X-ray emission associated with the Leo II group but did not resolve individual galaxies. Recently, using *Chandra* X-ray data, Jang et al. (2014) observed X-ray emission

from the central AGN in NGC 3607 and diffuse emission around NGC 3608. The detection of extended X-ray emissions confirms the presence of hot intergalactic gas.

The misalignment in the position angles of the GCs relative to the galaxy in NGC 3608 might be another sign of interaction with NGC 3607. Additionally, each galaxy shows an overabundance of GCs in the direct of the other, again suggesting a possible interaction between them. Jędrzejewski & Schechter (1988) proposed a close encounter between these two galaxies. They studied the absorption line kinematics for the stellar component of NGC 3608 and found a change in direction of the rotation curve between the core and outside region. They proposed that the reversal might be due to an interaction with the nearby NGC 3607.

We conclude that our results also support a possible interaction between the two galaxies. To confirm this proposition, deep surface photometric and detailed kinematic studies are needed.

6.5.2 Formation scenarios

As described in the introduction, three ‘classic’ formation scenarios were proposed to explain bimodality in GC systems. In the major merger model (Ashman & Zepf 1992), the blue GCs already exist in the merging galaxies, while the red GCs form during the merging process. In the multi-phase collapse scenario (Forbes et al. 1997), the blue GCs are formed early, followed by a quiescent phase. After a few Gyr, star formation is restarted with the formation of red GCs, which can be followed by accretion of additional blue GCs. According to Côté et al. (1998, 2000), the red GCs are inherent to the parent galaxies and the blue GCs are purely accreted from dwarf galaxies.

The three classic scenarios were explored in cosmological simulations which addressed a variety of GC system properties: structural and kinematical (Bekki et al. 2005), dynamical and chemical (Bekki et al. 2008), colour and metallicity bimodality (Muratov & Gnedin 2010; Tonini 2013), as well as physical relationships with the host galaxies (Beasley et al. 2002). Recently, Trenti et al. (2015) proposed another scenario for GC formation from the merging of multiple gas-rich mini haloes.

In all the classic formation scenarios, there is a strong association between red GC subpopulations and the parent galaxy. This relationship is established from different observations such as the strong relation between red GC peak colour and galaxy luminosity (Peng et al. 2006; Strader et al. 2006; Faifer et al. 2011), position angle arrangement of red GCs and the galaxy stellar component (Wang et al. 2013), connection between rotation velocity for red GCs and field stars (Pota et al. 2013), etc. On the other hand, the association between blue GC subpopulations and parent galaxy stars is weak. Peacock et al. (2015) found that the blue GC subpopulations of NGC 3115 are consistent with the stellar halo in metallicity and spatial distributions. However, the origin of the blue GC subpopulation is quite controversial. Côté et al. (1998, 2000) and Tonini (2013) proposed a dissipationless accretion origin, whereas dissipational *in situ* formation (Forbes et al. 1997; Beasley et al. 2003) is suggested for the formation of blue GCs in the inner regions. This distinction in region (inner or outer) is mentioned since accretion of blue GCs to the galaxy outskirts in the later phase is also included in the multi-phase scenario (Forbes et al. 1997).

Strader, Brodie & Forbes (2004) and Strader et al. (2005) investigated the feasibility of the above formation scenarios using observational data for massive elliptical galaxies. From the GC colour–galaxy luminosity relation and the age–metallicity relation,

they proposed an *in situ* plus accretion model for the formation of inner blue GCs which were then truncated by reionization, whereas the red GCs formed along with the bulk of field stars. They suggested that dwarf galaxies residing in overdense regions collapse before dwarfs in less dense regions, and then accrete more enriched gas from nearby star-forming regions. These dwarf galaxies, along with their blue GCs, are later accreted into the halo of a massive galaxy forming part of the main system. This implies an *in situ*+accretion origin for blue GCs. Hence, the origin of blue GCs in the inner regions could be due to one of three proposed processes, i.e. completely *in situ*, fully accreted or *in situ*+accretion.

In the following paragraphs, we try to differentiate between these three formation processes for blue GCs based on their global properties. In particular, we measure radial density, radial colour and azimuthal distributions in relation to their parent galaxies.

From the azimuthal distribution of GC subpopulations, both blue and red GCs have a positional arrangement in common with the galaxy stellar light component (Wang et al. 2013). This suggests that the blue GC subpopulation and galaxy stellar component have similar evolutionary histories. For galaxies in which the blue GCs and stars accreted from satellite dwarfs, this similarity is expected (Côté et al. 2001). From the derived ellipticities, it is seen that red GC subpopulations have a one-to-one relation with the galaxy stellar component, whereas the relation is not tight for blue GC subpopulations (see Fig. 17). If the galaxy has accreted its blue GCs recently, then a complete one-to-one correlation with host galaxy properties is not expected. Park & Lee (2013) also investigated this relationship for 23 ETGs using ACSVCS data and found an approximate one-to-one relation between blue GC ellipticity and the galaxy stellar component. As is well known, the ACS field of view does not provide anywhere near-complete coverage for massive nearby galaxies (Peng et al. 2006). That means a nearly one-to-one relation between inner blue GCs and galaxy stellar component suggests a common origin for both and hence supports the *in situ* formation scenario.

Another diagnostic trend is the GC subpopulation peak colour versus galaxy luminosity. The peak colour of the red GC subpopulation gets redder with increasing galaxy luminosity. Perhaps a weaker correlation exists for the blue GC subpopulation. Liu et al. (2011) found that projection effects tend to flatten GC radial trends, particularly for the blue subpopulation because of its extended nature. Hence, the slope of the relation between the blue GC subpopulation peak colour and galaxy luminosity is reduced to half of the earlier value (-0.0126 ± 0.0025 ; Peng et al. 2006), making the relation between peak colour of the blue GC subpopulation and galaxy luminosity insignificant. This result weakens the idea that the formation of blue GCs is via *in situ* processes.

Radial colour gradients may also reveal the origin of blue GCs. The colour gradients for blue GCs formed *in situ* are expected to be steeper than for a subpopulation formed from *in situ*+accretion or completely accreted processes. We expect this because the addition of GCs through accretion can dilute (in the case of *in situ*+accretion) the existing colour gradient for the blue GC subpopulation. In the case of complete accretion, we assume zero colour gradient for the blue subpopulation. Hence, to disentangle the origin of blue GCs, the steepness of the gradient needs to be quantified with large samples of galaxies where the colour gradients are measured with maximum accuracy. Our present work is limited by a small sample of 10 galaxies collected from the literature (Geisler et al. 1996; Bassino et al. 2006b; Harris 2009; Arnold et al. 2011; Faifer et al. 2011; Forbes et al. 2011; Blom et al. 2012; Usher et al. 2013; Hargis & Rhode 2014) and two from this work. Liu et al. (2011) carried

out an analysis of the colour gradients for 76 ETGs using ACSVCS and ACS Fornax Cluster Survey. Even though the sample size is impressive, only three galaxies have more than one pointing and we have included them in the above sample. Hence, significant colour gradients are detected in a total of 12 galaxies, 5 of which have multiple measurement. Gradient values are provided in Table 7.

Fig. 18 shows this sample of GC metallicity gradients plotted against host galaxy stellar mass. The blue GC subpopulation shows a trend of decreasing gradient with increasing galaxy stellar mass. This implies that high-mass galaxies have shallower gradients, whereas low-mass ($\log(M_*) \sim 11.0 M_\odot$) galaxies have steeper gradients. As the metallicity gradients show a dependence on galaxy stellar mass, both the GC subpopulations are expected to have some formational similarities with the galaxy stellar component. This means that a completely accreted origin (Côté et al. 1998, 2000; Tonini 2013) may not be the best scenario to explain the formation of blue GCs. Also, we notice that both GC subpopulation gradients show a dependence on galaxy stellar mass. Thus, a common or *in situ* origin (Forbes et al. 1997; Beasley et al. 2003) is probably involved in the formation of blue and red GC subpopulations (Pastorello et al. 2015). However, we note that large red (early-type) galaxies tend to preferentially accrete red satellite galaxies (Hearin et al. 2014; Hudson et al. 2015). Thus, GC system metallicity gradients may also reflect the gradients of the accreted satellites, if they are preserved in the accretion process. In the *in situ*+accretion formation scenario (Strader et al. 2004, 2005) for the blue GCs, we expect the gradient to be shallower than for the blue GCs formed completely *in situ*, but a reference scale is not yet established by models.

To summarize, from the present study it is difficult to ascribe either a completely *in situ* or an *in situ*+accretion origin for the blue GC subpopulations. A homogeneous large sample with accurate GC properties is needed to address this issue in depth.

7 CONCLUSIONS

We present wide-field imaging data from the Subaru telescope with which we carry out an investigation of the GC systems in the Leo II group to large galactocentric radii (~ 120 kpc). Using the multi-band wide-field images in *g*, *r* and *i* filters, we analysed the radial density, radial colour and azimuthal distributions of GC systems in the two brightest galaxies of the group, NGC 3607 and NGC 3608. Our study is complemented with spectroscopic data obtained from DEIMOS on the Keck II telescope. We present the main conclusions here.

(i) The GC systems of NGC 3607 and NGC 3808 are found to have radial extents of 9.5 ± 0.6 arcmin (equivalent to 61 ± 5 kpc or $\sim 4.4 R_e$) and 6.6 ± 0.8 arcmin (equivalent to 43 ± 5 kpc or $\sim 4.7 R_e$), respectively. The derived values are in agreement with estimates obtained from the empirical relation between the effective radius of the GC system and galaxy stellar light given in Kartha et al. (2014).

(ii) The GC system colours of both galaxies are fitted with the GMM algorithm, and we detect a bimodal distribution with confidence level greater than 99.99 per cent. NGC 3607 is observed to have 45 ± 9 and 55 ± 8 per cent of blue and red GC subpopulations, while for NGC 3608 the blue and red GC subpopulations contribute 65 ± 6 and 35 ± 6 per cent to the total GC system.

(iii) From the radial velocity measurements, we detect 81 GCs in the field of the Leo II group. We assign 46 and 35 GCs, respectively,

to NGC 3607 and NGC 3608. We estimate a mean velocity of 963 and 1220 km s⁻¹ for NGC 3607 and NGC 3608, respectively. Also, the mean GC velocity dispersions for the respective galaxies are 167 and 147 km s⁻¹.

(iv) From the radial density distributions of the GC subpopulations of NGC 3607, the red subpopulation is more centrally located while the blue subpopulation is more extended. Also, the effective radius of the red GC subpopulation (40 ± 29 arcsec) and the galaxy stellar light (39 arcsec) are in good agreement, compared to the blue subpopulation (95 ± 50 arcsec).

(v) For NGC 3608, the blue subpopulation is more extended in radius than the centrally concentrated red subpopulation. The red subpopulation distribution shows similarities with the galaxy surface brightness distribution. However, the effective radius of the red subpopulation (59 ± 40 arcsec) is larger than the galaxy stellar light (30 arcsec).

(vi) The azimuthal distribution of the NGC 3607 GC system reveals that both subpopulations are aligned along a position angle (~ 110 deg), which is in reasonable agreement with the galaxy stellar light (125 deg). However, the distribution of the GC system is more elliptical in comparison with the circular distribution of galaxy stellar light. The red subpopulation shows a more elliptical distribution when compared with the blue subpopulation.

(vii) For NGC 3608, the GCs are arranged along position angles that are different from the galaxy stellar population. Using two different methods of GC selection, the position angles for the total GC system are found to be along 104 ± 15 and 67 ± 7 deg, while the galaxy major axis is at 82 deg. One method of GC selection suggests that the GCs have an ellipticity = 0.20 ± 0.09 , while the other shows an ellipticity of 0.39 ± 0.10 . By comparison, the stellar light ellipticity is 0.20. In NGC 3608, the blue subpopulation has a more elliptical arrangement than the red subpopulation.

(viii) The total GC system, and both subpopulations of NGC 3607, becomes bluer in colour with increasing galactocentric radius; a significant metallicity gradient is observed for both subpopulations. We find that the blue subpopulation has a steeper gradient than the red subpopulation. We also detect a strong colour gradient only for the blue subpopulation of NGC 3608. The colour gradient for the blue subpopulation in NGC 3608 is steeper than that in NGC 3607.

We compare different global properties of the GC systems and their parent galaxies. We reconfirm that the extent of the GC system is a function of galaxy size, and the effective radius of a GC system is nearly six times the effective radius of parent galaxy. We obtain a one-to-one relation between the parent red GC ellipticities and galaxy stellar light ellipticities. Also, the blue GC ellipticities of slow rotators with kinematically decoupled cores are more elongated than their red GC subpopulation ellipticities. We propose that they might have experienced recent minor mergers from anisotropic directions (Tempel et al. 2015).

From a sample of 12 galaxies, we investigate the relationship between the metallicity gradients and host galaxy stellar mass. We found that the gradients of both GC subpopulations become shallower with increasing stellar mass. The average ratio of blue to red GCs in galaxies in the mass range $11.0 < \log(M_*) < 12.0 M_\odot$ is nearly 1.7. These findings agree with the predictions from the simulations of Bekki et al. (2008) and also with the findings from other observations (Peng et al. 2006). We also carried out a study to disentangle the formation of blue GC subpopulations (i.e. completely *in situ* versus *in situ*+accretion versus completely accreted), which

have not given conclusive results and need to be followed up with a homogeneous, large sample.

ACKNOWLEDGEMENTS

We thank the anonymous referee for his/her careful reading of the manuscript and the valuable feedbacks. We extend our gratitude to Jacob A. Arnold and Kristin A. Woodley regarding their help in observations. We thank Blesson Mathew and Nicola Pastorello for the careful reading of the manuscript. We also acknowledge the members of SAGES group, especially Christopher Usher, Vincenzo Pota and Joachim Janz, for the support and enlightening discussions. SSK thanks the Swinburne University for the SUPRA fellowship. DAF thanks the ARC for support via DP-130100388. This work was supported by NSF grant AST-1211995. This paper was based in part on data collected at Subaru Telescope, which is operated by the National Astronomical Observatory of Japan. This paper uses data products produced by the OIR Telescope Data Center, supported by the Smithsonian Astrophysical Observatory. This work is based on observations made with the NASA/ESA *Hubble Space Telescope*, and obtained from the Hubble Legacy Archive, which is a collaboration between the Space Telescope Science Institute (STScI/NASA), the Space Telescope European Coordinating Facility (ST-ECF/ESA) and the Canadian Astronomy Data Centre (CADM/NRC/CSA). Some of the data presented herein were obtained at the W. M. Keck Observatory, operated as a scientific partnership among the California Institute of Technology, the University of California and the National Aeronautics and Space Administration, and made possible by the generous financial support of the W. M. Keck Foundation. We wish to recognize and acknowledge the very significant cultural role and reverence that the summit of Mauna Kea has always had within the indigenous Hawaiian community. We are most fortunate to have the opportunity to conduct observations from this mountain. This research has made use of the NASA/IPAC Extragalactic Database (NED) operated by the Jet Propulsion Laboratory, California Institute of Technology, under contract with the National Aeronautics and Space Administration. The analysis pipeline used to reduce the DEIMOS data was developed at UC Berkeley with support from NSF grant AST-0071048. We acknowledge the usage of the HyperLeda data base (<http://leda.univ-lyon1.fr>).

REFERENCES

- Alamo-Martínez K. A. et al., 2012, *A&A*, 546, A15
 Annibali F., Bressan A., Rampazzo R., Zeilinger W. W., Danese L., 2007, *A&A*, 463, 455
 Arnold J. A., Romanowsky A. J., Brodie J. P., Chomiuk L., Spitler L. R., Strader J., Benson A. J., Forbes D. A., 2011, *ApJ*, 736, L26
 Ashman K. M., Zepf S. E., 1992, *ApJ*, 384, 50
 Bassino L. P., Richtler T., Dirsch B., 2006a, *MNRAS*, 367, 156
 Bassino L. P., Faifer F. R., Forte J. C., Dirsch B., Richtler T., Geisler D., Schuberth Y., 2006b, *A&A*, 451, 789
 Beasley M. A., Baugh C. M., Forbes D. A., Sharples R. M., Frenk C. S., 2002, *MNRAS*, 333, 383
 Beasley M. A., Harris W. E., Harris G. L. H., Forbes D. A., 2003, *MNRAS*, 340, 341
 Bekki K., Beasley M. A., Brodie J. P., Forbes D. A., 2005, *MNRAS*, 363, 1211
 Bekki K., Yahagi H., Nagashima M., Forbes D. A., 2008, *MNRAS*, 387, 1131
 Bell E. F., McIntosh D. H., Katz N., Weinberg M. D., 2003, *ApJS*, 149, 289
 Bertin E., Arnouts S., 1996, *A&AS*, 117, 393
 Blom C., Spitler L. R., Forbes D. A., 2012, *MNRAS*, 420, 37
 Brodie J. P., Strader J., 2006, *ARA&A*, 44, 193
 Brodie J. P., Romanowsky A. J., Strader J., Forbes D. A., 2011, *AJ*, 142, 199
 Brodie J. P., Usher C., Conroy C., Strader J., Arnold J. A., Forbes D. A., Romanowsky A. J., 2012, *ApJ*, 759, L33
 Brodie J. P. et al., 2014, *ApJ*, 796, 52
 Cantiello M. et al., 2015, *A&A*, 576, A14
 Cappellari M. et al., 2011, *MNRAS*, 413, 813
 Cappellari M. et al., 2013, *MNRAS*, 432, 1862
 Coccato L. et al., 2009, *MNRAS*, 394, 1249
 Côté P., Marzke R. O., West M. J., 1998, *ApJ*, 501, 554
 Côté P., Marzke R. O., West M. J., Minniti D., 2000, *ApJ*, 533, 869
 Côté P. et al., 2001, *ApJ*, 559, 828
 de Vaucouleurs G., de Vaucouleurs A., Corwin H. G., Jr, Buta R. J., Paturel G., Fouqué P., 1991, *Third Reference Catalogue of Bright Galaxies. Volume I: Explanations and References. Volume II: Data for Galaxies between 0^h and 12^h. Volume III: Data for Galaxies between 12^h and 24^h*. Springer, NY
 Di Matteo P., Pipino A., Lehnert M. D., Combes F., Semelin B., 2009, *A&A*, 499, 427
 Dirsch B., Schuberth Y., Richtler T., 2005, *A&A*, 433, 43
 Dotter A. et al., 2010, *ApJ*, 708, 698
 Duc P.-A. et al., 2015, *MNRAS*, 446, 120
 Emsellem E. et al., 2011, *MNRAS*, 414, 888
 Faber S. M. et al., 2003, in Iye M., Moorwood A. F. M., eds, *Proc. SPIE Conf. Ser. Vol. 4841, Instrument Design and Performance for Optical/Infrared Ground-Based Telescopes*. SPIE, Bellingham, p. 1657
 Faifer F. R. et al., 2011, *MNRAS*, 416, 155
 Forbes D. A., Forte J. C., 2001, *MNRAS*, 322, 257
 Forbes D. A., Brodie J. P., Grillmair C. J., 1997, *AJ*, 113, 1652
 Forbes D. A. et al., 2006a, *PASA*, 23, 38
 Forbes D. A., Sánchez-Blázquez P., Phan A. T. T., Brodie J. P., Strader J., Spitler L., 2006b, *MNRAS*, 366, 1230
 Forbes D. A., Spitler L. R., Strader J., Romanowsky A. J., Brodie J. P., Foster C., 2011, *MNRAS*, 413, 2943
 Forbes D. A., Ponman T., O’Sullivan E., 2012, *MNRAS*, 425, 66
 Forbes D. A., Pastorello N., Romanowsky A. J., Usher C., Brodie J. P., Strader J., 2015, *MNRAS*, 452, 1045
 Forte J. C., Vega E. I., Faifer F., 2012, *MNRAS*, 421, 635
 Geisler D., Lee M. G., Kim E., 1996, *AJ*, 111, 1529
 Gnedin O. Y., Ostriker J. P., Tremaine S., 2014, *ApJ*, 785, 71
 Graham A. W., Driver S. P., 2005, *PASA*, 22, 118
 Griffen B. F., Drinkwater M. J., Thomas P. A., Helly J. C., Pimblett K. A., 2010, *MNRAS*, 405, 375
 Hargis J. R., Rhode K. L., 2014, *ApJ*, 796, 62
 Harris W. E., 2009, *ApJ*, 703, 939
 Harris W. E., 2010, *Phil. Trans. R. Soc. A*, 368, 889
 Harris W. E., Kavelaars J. J., Hanes D. A., Hesser J. E., Pritchett C. J., 2000, *ApJ*, 533, 137
 Hearin A. P., Watson D. F., Becker M. R., Reyes R., Berlind A. A., Zentner A. R., 2014, *MNRAS*, 444, 729
 Hirschmann M., Naab T., Ostriker J. P., Forbes D. A., Duc P.-A., Davé R., Oser L., Karabal E., 2015, *MNRAS*, 449, 528
 Hopkins P. F., Cox T. J., Dutta S. N., Hernquist L., Kormendy J., Lauer T. R., 2009, *ApJS*, 181, 135
 Hudson M. J. et al., 2015, *MNRAS*, 447, 298
 Jang I., Gliozzi M., Hughes C., Titarchuk L., 2014, *MNRAS*, 443, 72
 Jarrett T. H., Chester T., Cutri R., Schneider S., Skrutskie M., Huchra J. P., 2000, *AJ*, 119, 2498
 Jedrzejewski R., Schechter P. L., 1988, *ApJ*, 330, L87
 Kartha S. S., Forbes D. A., Spitler L. R., Romanowsky A. J., Arnold J. A., Brodie J. P., 2014, *MNRAS*, 437, 273
 Katz H., Ricotti M., 2013, *MNRAS*, 432, 3250
 Kim H.-S., Yoon S.-J., Sohn S. T., Kim S. C., Kim E., Chung C., Lee S.-Y., Lee Y.-W., 2013, *ApJ*, 763, 40
 Krajnović D. et al., 2011, *MNRAS*, 414, 2923
 Kron R. G., 1980, *ApJS*, 43, 305
 Kundu A., Whitmore B. C., 2001a, *AJ*, 121, 2950

- Kundu A., Whitmore B. C., 2001b, *AJ*, 122, 1251
 Larsen S. S., Brodie J. P., Huchra J. P., Forbes D. A., Grillmair C. J., 2001, *AJ*, 121, 2974
 Lauer T. R. et al., 2005, *AJ*, 129, 2138
 Li H., Gnedin O. Y., 2014, *ApJ*, 796, 10
 Liu C., Peng E. W., Jordán A., Ferrarese L., Blakeslee J. P., Côté P., Mei S., 2011, *ApJ*, 728, 116
 McDermid R. M. et al., 2015, *MNRAS*, 448, 3484
 McLaughlin D. E., Harris W. E., Hanes D. A., 1994, *ApJ*, 422, 486
 Maraston C., 2005, *MNRAS*, 362, 799
 Miyazaki S. et al., 2002, *PASJ*, 54, 833
 Mulchaey J. S., Davis D. S., Mushotzky R. F., Burstein D., 2003, *ApJS*, 145, 39
 Muratov A. L., Gnedin O. Y., 2010, *ApJ*, 718, 1266
 Naab T. et al., 2014, *MNRAS*, 444, 3357
 Oser L., Ostriker J. P., Naab T., Johansson P. H., Burkert A., 2010, *ApJ*, 725, 2312
 Ouchi M. et al., 2004, *ApJ*, 611, 660
 Park H. S., Lee M. G., 2013, *ApJ*, 773, L27
 Pastorello N. et al., 2015, *MNRAS*, 451, 2625
 Paturel G., Petit C., Prugniel P., Theureau G., Rousseau J., Brouty M., Dubois P., Cambrésy L., 2003, *A&A*, 412, 45
 Peacock M. B., Strader J., Romanowsky A. J., Brodie J. P., 2015, *ApJ*, 800, 13
 Peng E. W. et al., 2006, *ApJ*, 639, 95
 Pipino A., D’Ercole A., Chiappini C., Matteucci F., 2010, *MNRAS*, 407, 1347
 Pota V. et al., 2013, *MNRAS*, 428, 389
 Rhode K. L., Windschitl J. L., Young M. D., 2010, *AJ*, 140, 430
 Rickes M. G., Pastoriza M. G., Bonatto C., 2009, *A&A*, 505, 73
 Schlegel D. J., Finkbeiner D. P., Davis M., 1998, *ApJ*, 500, 525
 Spitler L. R., 2010, *MNRAS*, 406, 1125
 Spitler L. R., Larsen S. S., Strader J., Brodie J. P., Forbes D. A., Beasley M. A., 2006, *AJ*, 132, 1593
 Spitler L. R., Forbes D. A., Strader J., Brodie J. P., Gallagher J. S., 2008, *MNRAS*, 385, 361
 Stoughton C. et al., 2002, *AJ*, 123, 485
 Strader J., Brodie J. P., Forbes D. A., 2004, *AJ*, 127, 3431
 Strader J., Brodie J. P., Cenarro A. J., Beasley M. A., Forbes D. A., 2005, *AJ*, 130, 1315
 Strader J., Brodie J. P., Spitler L., Beasley M. A., 2006, *AJ*, 132, 2333
 Strader J. et al., 2011, *ApJS*, 197, 33
 Strader J. et al., 2012, *ApJ*, 760, 87
 Tempel E., Guo Q., Kipper R., Libeskind N. I., 2015, *MNRAS*, 450, 2727
 Terlevich A. I., Forbes D. A., 2002, *MNRAS*, 330, 547
 Tonini C., 2013, *ApJ*, 762, 39
 Tortora C., Napolitano N. R., Cardone V. F., Capaccioli M., Jetzer P., Molinaro R., 2010, *MNRAS*, 407, 144
 Trenti M., Padoan P., Jimenez R., 2015, *ApJL*, 808, 35
 Tully R. B., 1988, *Nearby Galaxies Catalog*. Cambridge Univ. Press, Cambridge
 Usher C. et al., 2012, *MNRAS*, 426, 1475
 Usher C., Forbes D. A., Spitler L. R., Brodie J. P., Romanowsky A. J., Strader J., Woodley K. A., 2013, *MNRAS*, 436, 1172
 Walker M. G., Mateo M., Olszewski E. W., Pal J. K., Sen B., Woodroffe M., 2006, *ApJ*, 642, L41
 Wang Q., Peng E. W., Blakeslee J. P., Côté P., Ferrarese L., Jordán A., Mei S., West M. J., 2013, *ApJ*, 769, 145
 Zepf S. E., Ashman K. M., 1993, *MNRAS*, 264, 611

APPENDIX A: LIST OF SPECTROSCOPICALLY CONFIRMED OBJECTS AROUND THE LEO II GROUP

Table A1 presents the photometric magnitudes g , r and i and the radial velocities for GCs, Galactic stars and background galaxies detected around NGC 3607 and NGC 3608 in the Leo II group.

Table A1. Catalogue of objects detected around NGC 3607 and NGC 3608. The horizontal lines differentiate GCs of NGC 3607, GCs of NGC 3608, seven ambiguous objects (classified into GCs and probable UCD – see Section 4.3), Galactic stars and background galaxies. Column 1 represents the object ID with the galaxy name followed by the object classification such as GC, star and galaxy. Columns 2 and 3 present the position in right ascension and declination (J2000). Columns 4–9 present the Subaru/Suprime-Cam photometry in g , r and i filters and their respective uncertainties (given here are extinction-corrected magnitudes). The heliocentric velocity and the respective uncertainty for each object are given in columns 10 and 11.

ID	RA (deg)	Dec. (deg)	g (mag)	δg (mag)	r (mag)	δr (mag)	i (mag)	δi (mag)	V_{rad} (km s ⁻¹)	δV (km s ⁻¹)
(1)	(2)	(3)	(4)	(5)	(6)	(7)	(8)	(9)	(10)	(11)
NGC 3607_GC1	169.217 229	18.003 300	22.320	0.002	21.863	0.003	21.653	0.003	958	14
NGC 3607_GC2	169.231 425	18.022 400	22.782	0.003	22.019	0.003	21.622	0.003	924	9
NGC 3607_GC3	169.298 829	18.025 774	22.706	0.004	22.228	0.003	22.027	0.004	1255	13
NGC 3607_GC4	169.268 788	18.026 516	22.646	0.003	21.898	0.002	21.533	0.003	910	12
NGC 3607_GC5	169.247 763	18.029 331	21.396	0.001	20.756	0.001	20.492	0.001	904	5
NGC 3607_GC6	169.239 792	18.027 800	22.370	0.002	21.734	0.002	21.477	0.003	825	15
NGC 3607_GC7	169.201 883	18.032 566	23.010	0.003	22.235	0.003	21.837	0.003	961	17
NGC 3607_GC8	169.251 525	18.034 105	22.218	0.002	21.596	0.002	21.361	0.002	732	13
NGC 3607_GC9	169.208 850	18.035 141	20.924	0.001	20.340	0.001	20.115	0.001	950	4
NGC 3607_GC10	169.230 150	18.037 170	22.053	0.002	21.321	0.002	21.027	0.002	924	15
NGC 3607_GC11	169.199 067	18.037 264	23.225	0.004	22.434	0.004	22.066	0.004	1136	15
NGC 3607_GC12	169.159 492	18.033 494	24.264	0.011	23.764	0.014	23.499	0.014	1052	12
NGC 3607_GC13	169.236 067	18.038 172	22.161	0.002	21.525	0.002	21.279	0.002	792	13
NGC 3607_GC14	169.099 217	18.039 568	22.358	0.002	21.732	0.002	21.482	0.002	1048	15
NGC 3607_GC15	169.207 533	18.043 100	23.017	0.004	22.368	0.004	22.065	0.004	764	17
NGC 3607_GC16	169.213 671	18.044 300	23.698	0.005	23.089	0.006	22.770	0.007	1060	14
NGC 3607_GC17	169.237 692	18.047 800	21.814	0.001	21.057	0.001	20.719	0.001	920	12
NGC 3607_GC18	169.238 979	18.049 000	23.307	0.007	22.484	0.007	21.903	0.006	1092	13
NGC 3607_GC19	169.184 475	18.049 648	22.226	0.002	21.579	0.003	21.377	0.002	966	13
NGC 3607_GC20	169.194 458	18.052 082	22.753	0.003	22.098	0.003	21.713	0.004	974	14
NGC 3607_GC21	169.240 721	18.054 500	21.360	0.001	20.738	0.001	20.463	0.001	598	9
NGC 3607_GC22	169.220 738	18.047 815	21.831	0.001	21.313	0.001	21.092	0.002	1303	19

Table A1. – continued.

ID	RA	Dec.	g	δg	r	δr	i	δi	V_{rad}	δV
(1)	(deg)	(deg)	(mag)	(mag)	(mag)	(mag)	(mag)	(mag)	(km s^{-1})	(km s^{-1})
(1)	(2)	(3)	(4)	(5)	(6)	(7)	(8)	(9)	(10)	(11)
NGC 3607_GC23	169.242 683	18.055 283	21.524	0.001	20.757	0.001	20.448	0.001	840	9
NGC 3607_GC24	169.265 371	18.060 005	22.899	0.003	22.149	0.003	21.811	0.003	1027	11
NGC 3607_GC25	169.232 196	18.058 500	23.611	0.006	22.948	0.006	22.492	0.006	987	13
NGC 3607_GC26	169.271 792	18.065 065	23.112	0.004	22.420	0.004	22.110	0.004	1025	12
NGC 3607_GC27	169.186 392	18.065 200	21.930	0.002	21.293	0.003	21.060	0.003	848	16
NGC 3607_GC28	169.219 979	18.068 300	21.646	0.001	20.972	0.001	20.655	0.001	835	6
NGC 3607_GC29	169.237 104	18.074 398	22.956	0.004	22.211	0.004	21.830	0.004	958	16
NGC 3607_GC30	169.213 671	18.076 300	24.242	0.009	23.568	0.009	23.240	0.01	1012	12
NGC 3607_GC31	169.308 429	18.075 178	23.142	0.004	22.514	0.004	22.248	0.005	949	14
NGC 3607_GC32	169.229 092	18.086 800	22.753	0.003	22.003	0.003	21.650	0.003	815	9
NGC 3607_GC33	169.212 542	18.087 000	21.839	0.001	21.158	0.001	20.890	0.002	985	7
NGC 3607_GC34	169.160 442	18.106 018	22.294	0.002	21.748	0.002	21.521	0.003	694	9
NGC 3607_GC35	169.106 842	18.140 724	23.123	0.004	22.499	0.004	22.267	0.005	1138	18
NGC 3607_GC36	169.376 407	18.206 726	22.467	0.002	21.941	0.003	21.741	0.003	1106	14
NGC 3607_GC37	169.189 700	18.011 189	23.796	0.005	23.047	0.005	22.757	0.006	723	17
NGC 3607_GC38	169.211 025	18.018 753	22.581	0.002	22.030	0.003	21.810	0.003	940	18
NGC 3607_GC39	169.222 354	18.045 021	21.901	0.001	21.198	0.001	20.898	0.001	1145	23
NGC 3607_GC40	169.203 471	18.038 366	22.804	0.004	22.081	0.004	21.699	0.004	775	14
NGC 3607_GC41	169.233 100	18.040 434	22.867	0.003	22.145	0.003	21.782	0.003	873	26
NGC 3607_GC42	169.242 008	18.074 684	24.662	0.013	24.083	0.016	23.961	0.018	1188	19
NGC 3607_GC43	169.107 099	18.244 194	22.618	0.003	22.043	0.003	21.819	0.003	1279	16
NGC 3608_GC1	169.231 942	18.129 700	25.547	0.021	24.951	0.023	24.783	0.028	1039	13
NGC 3608_GC2	169.246 717	18.131 090	22.657	0.003	22.041	0.003	21.806	0.003	1293	13
NGC 3608_GC3	169.261 129	18.135 875	21.721	0.001	21.065	0.001	20.849	0.001	1091	6
NGC 3608_GC4	169.227 192	18.138 500	21.595	0.001	20.916	0.001	20.648	0.001	1272	8
NGC 3608_GC5	169.298 158	18.138 886	22.732	0.003	22.140	0.003	21.918	0.003	1242	15
NGC 3608_GC6	169.245 833	18.146 111	23.950	0.007	23.105	0.006	22.668	0.006	1176	29
NGC 3608_GC7	169.269 692	18.139 126	22.568	0.002	21.890	0.003	21.623	0.003	1458	9
NGC 3608_GC8	169.263 733	18.142 671	24.392	0.009	23.568	0.009	23.227	0.009	1141	15
NGC 3608_GC9	169.224 058	18.145 254	22.229	0.002	21.650	0.002	21.418	0.002	1493	14
NGC 3608_GC10	169.241 266	18.144 31	21.213	0.001	20.639	0.001	20.371	0.001	1203	12
NGC 3608_GC11	169.275 825	18.151 506	24.155	0.011	23.506	0.011	23.181	0.013	1467	19
NGC 3608_GC12	169.298 200	18.149 405	22.834	0.003	22.243	0.003	22.044	0.004	1061	12
NGC 3608_GC13	169.222 383	18.155 500	22.851	0.003	22.260	0.003	22.029	0.004	957	15
NGC 3608_GC14	169.243 342	18.156 600	22.166	0.002	21.581	0.002	21.258	0.002	1335	12
NGC 3608_GC15	169.229 208	18.167 700	23.038	0.003	22.479	0.003	22.272	0.004	1229	17
NGC 3608_GC16	169.324 208	18.163 569	22.591	0.002	21.995	0.003	21.763	0.003	1268	9
NGC 3608_GC17	169.260 221	18.165 211	22.266	0.002	21.670	0.002	21.487	0.002	1283	12
NGC 3608_GC18	169.273 496	18.165 411	23.057	0.005	22.558	0.005	22.414	0.005	1038	13
NGC 3608_GC19	169.292 936	18.166 916	21.915	0.002	21.332	0.002	21.130	0.002	1176	7
NGC 3608_GC20	169.229 207	18.167 725	22.623	0.002	21.976	0.002	21.741	0.003	1233	14
NGC 3608_GC21	169.252 583	18.168 700	22.874	0.003	22.248	0.004	22.035	0.004	1247	19
NGC 3608_GC22	169.320 831	18.169 830	22.265	0.002	21.576	0.002	21.289	0.002	1383	7
NGC 3608_GC23	169.337 812	18.171 459	22.885	0.003	22.267	0.004	22.031	0.004	1294	11
NGC 3608_GC24	169.220 495	18.173 113	23.444	0.006	22.925	0.005	22.703	0.006	1118	17
NGC 3608_GC25	169.259 806	18.179 447	22.292	0.003	21.759	0.003	21.582	0.003	1385	8
NGC 3608_GC26	169.237 946	18.138 157	23.728	0.005	22.946	0.005	22.619	0.005	1031	26
NGC 3608_GC27	169.271 321	18.159 868	23.265	0.004	22.567	0.004	22.266	0.004	808	22
NGC 3608_GC28	169.228 779	18.133 675	22.476	0.002	21.936	0.002	21.736	0.003	1358	17
NGC 3608_GC29	169.266 946	18.158 815	23.398	0.004	22.629	0.004	22.304	0.004	1076	18
NGC 3608_GC30	169.213 571	18.159 685	23.121	0.004	22.496	0.004	22.268	0.004	1238	25
NGC 3608_GC31	169.254 055	18.160 824	23.176	0.004	22.574	0.004	22.354	0.005	1328	12
NGC 3608_GC32	169.256 616	18.169 390	23.532	0.005	22.965	0.006	22.689	0.006	1180	19
NGC 3607_GC44	169.303 350	18.082 405	22.710	0.003	22.061	0.003	21.800	0.003	1318	11
NGC 3607_GC45	169.245 171	18.095 700	22.927	0.003	22.233	0.003	21.962	0.004	1089	14
NGC 3607_GC46	169.184 189	18.164 358	22.793	0.003	21.974	0.003	21.599	0.003	807	9
NGC 3608_GC33	169.203 088	18.135 864	22.218	0.002	21.563	0.002	21.314	0.002	1160	10
NGC 3608_GC34	169.217 304	18.109 472	22.905	0.004	22.333	0.004	22.084	0.005	1281	23
NGC 3608_GC35	169.192 558	18.121 163	23.079	0.004	22.484	0.004	22.250	0.005	1229	18
NGC 3608_ext1	169.197 333	18.036 472	22.384	0.0020	21.893	0.0020	21.761	0.0030	1822	22
NGC 3608_star1	169.181 300	18.000 490	22.633	0.002	22.119	0.003	21.950	0.003	113	11

Table A1. – *continued.*

ID	RA	Dec.	g	δg	r	δr	i	δi	V_{rad}	δV
(1)	(deg)	(deg)	(mag)	(mag)	(mag)	(mag)	(mag)	(mag)	(km s ⁻¹)	(km s ⁻¹)
(1)	(2)	(3)	(4)	(5)	(6)	(7)	(8)	(9)	(10)	(11)
NGC 3608_star2	169.189 558	18.004 114	21.235	0.001	20.761	0.001	20.625	0.001	-106	7
NGC 3608_star3	169.223 729	18.025 229	25.096	0.017	24.464	0.018	24.073	0.019	26	4
NGC 3608_star4	169.106 475	18.053 684	25.544	0.032	24.902	0.031	24.719	0.039	90	10
NGC 3608_star5	169.109 129	18.074 558	21.437	0.001	20.954	0.001	20.821	0.002	-37	10
NGC 3608_star6	169.293 779	18.109 633	21.351	0.001	20.865	0.001	20.739	0.001	139	7
NGC 3608_star7	169.243 571	18.115 063	22.741	0.003	22.112	0.003	21.871	0.004	-59	17
NGC 3608_star8	169.251 296	18.129 112	22.151	0.002	21.527	0.002	21.315	0.002	159	11
NGC 3608_star9	169.198 996	18.147 369	21.484	0.001	20.985	0.001	20.849	0.002	87	9
NGC 3608_star10	169.148 208	18.176 922	25.108	0.030	24.433	0.033	24.134	0.027	-107	16
NGC 3608_star11	169.389 467	18.250 843	22.643	0.003	22.093	0.003	21.938	0.004	66	12
NGC 3608_gal1	169.295 992	18.040 196	22.481	0.003	21.922	0.003	21.613	0.003	-	-
NGC 3608_gal2	169.190 583	18.043 064	23.802	0.006	23.230	0.006	23.023	0.008	-	-
NGC 3608_gal3	169.076 800	18.045 994	23.127	0.004	22.546	0.004	22.340	0.005	-	-
NGC 3608_gal4	169.218 121	18.052 868	21.831	0.001	21.313	0.001	21.092	0.002	-	-
NGC 3608_gal5	169.111 229	18.095 403	25.878	0.043	25.324	0.056	24.929	0.056	-	-
NGC 3608_gal6	169.125 054	18.108 242	22.672	0.003	22.205	0.003	22.070	0.004	-	-
NGC 3608_gal7	169.289 267	18.119 137	25.637	0.025	24.959	0.032	24.744	0.040	-	-
NGC 3608_gal8	169.159 358	18.134 090	25.586	0.027	25.101	0.032	24.762	0.037	-	-
NGC 3608_gal9	169.115 850	18.138 969	21.265	0.001	20.782	0.001	20.536	0.002	-	-
NGC 3608_gal10	169.219 142	18.155 857	23.989	0.008	23.270	0.008	23.021	0.009	-	-
NGC 3608_gal11	169.245 833	18.148 889	22.166	0.002	21.581	0.002	21.258	0.002	-	-
NGC 3608_gal12	169.282 651	18.165 146	23.456	0.005	22.881	0.006	22.709	0.008	-	-
NGC 3608_gal13	169.273 496	18.165 411	23.057	0.005	22.558	0.005	22.414	0.005	-	-
NGC 3608_gal14	169.199 783	18.173 775	25.439	0.041	24.884	0.042	24.507	0.038	-	-
NGC 3608_gal15	169.210 004	18.011 913	23.890	0.007	23.230	0.008	22.909	0.009	-	-

APPENDIX B: M/L RATIO CALCULATION USING BELL ET AL. (2003)

Relationships between stellar M/L values and various colours in SDSS and 2MASS passbands are given in Bell et al. (2003). They derived these relationships by fitting galaxy evolution models to a large sample of 22 679 galaxies from the SDSS Early Data Release (Stoughton et al. 2002) and 2MASS extended source catalogue (Jarrett et al. 2000). To estimate the stellar mass for our sample of 42 galaxies, we utilize the relationship between M/L ratio and $(B - V)$ colour which is given as

$$\log_{10}(M/L) = -0.628 + (1.305 \times (B - V)). \quad (\text{B1})$$

We find that the Bell et al. (2003) M/L ratios are about a factor of ~ 2 lower for ellipticals and a factor of ~ 1.5 lower for lenticulars than Zepf & Ashman (1993) values. This affects the X -axes of Figs 18 and 20. Hence, we fit the trends in Fig. 18 after incorporating the stellar mass from Bell et al. (2003). The fits are given below which can be compared to equations (7)–(9):

$$\Delta[Z/H]_{\text{BGC}} = [(0.33 \pm 0.07) \times \log(M_*)] - (3.9 \pm 0.8) \quad (\text{B2})$$

$$\Delta[Z/H]_{\text{RGC}} = [(0.0007 \pm 0.06) \times \log(M_*)] - (0.15 \pm 0.9) \quad (\text{B3})$$

$$\Delta[Z/H]_{\text{RGC}} = [(0.07 \pm 0.05) \times \log(M_*)] - (0.89 \pm 0.75). \quad (\text{B4})$$

We find that even if the stellar mass varies between Zepf & Ashman (1993) and Bell et al. (2003), the relationship shown by blue and red GCs with metallicity remains statistically the same. This also implies that our results remain unchanged between different M/L ratio estimations.

This paper has been typeset from a $\text{\TeX}/\text{\LaTeX}$ file prepared by the author.